Finescale Vertical Structure and Evolution of a Preconvective Dryline on 19 June 2002

BENJAMIN D. SIPPRELL AND BART GEERTS

University of Wyoming, Laramie, Wyoming

(Manuscript received 9 January 2006, in final form 17 July 2006)

ABSTRACT

High-resolution airborne cloud radar data and other International H_2O Project datasets are used to describe the vertical structure of an unusual prefrontal dryline. This dryline, observed in northwestern Kansas on 19 June 2002, first progressed eastward and tilted toward the west, and later became more stationary and reversed its tilt, toward the moist side. The convective boundary layer (CBL) depth difference also reversed: only in the later phase did the dry-side CBL become deeper than on the moist side. Echo and single/dual-Doppler velocity data in a vertical transect across the dryline suggest a solenoidal circulation dynamically consistent with the observed horizontal buoyancy gradient. Both this gradient and the solenoidal circulation reversed in the later phase. Simultaneously, confluence toward the dryline increased, resulting in an increasing moisture gradient as well as a deepening CBL in the dryline convergence zone. It is speculated that the baroclinically generated horizontal vorticity contributed to this CBL deepening, as the sign of this vorticity was opposite to that of the low-level wind shear on the opposite side of the dryline in both phases. Deep-convective initiation appears to have resulted from this local CBL deepening, leading to a total elimination of convective inhibition near the dryline.

1. Introduction

The formation of drylines is a well known yet still poorly understood factor in the initiation of deep convection [referred to as convection initiation (CI)]. Notwithstanding much observational research (Mahrt 1977; McCarthy and Koch 1982; Koch and McCarthy 1982; Wilson and Schreiber 1986; Parsons et al. 1991; Lee et al. 1991; Wilson et al. 1992; Hane et al. 1993; Ziegler and Hane 1993; Fankhauser et al. 1995; Hane et al. 1997; Crawford and Bluestein 1997; Atkins et al. 1998; Ziegler and Rasmussen 1998; Hane et al. 2002) and modeling studies (Sun and Ogura 1979; Ziegler et al. 1995; Crook 1996; Shaw et al. 1997; Ziegler et al. 1997), questions remain about how both mesoscale and finer-scale atmospheric processes generate and sustain a dryline in the convective boundary layer (CBL), and how deep convection erupts along a dryline.

Certainly larger-scale variations in terrain, land surface conditions, as well as the diurnally varying low-level pressure and wind patterns, are essential to the background humidity gradient (e.g., Schaefer 1974; Sun and Wu 1992; Jones and Bannon 2002), but convergence tends to occur at rather small scales (e.g., Ziegler et al. 1995; Shaw et al. 1997; Atkins et al. 1998), sometimes leading to several dryline boundaries (e.g., Hane et al. 2002). A dryline is typically characterized by a sharp moisture contrast collocated with a low-level convergence maximum. The convergence supports rising motion and progressive deepening of the CBL, especially when the CBL is weakly capped and the highest virtual potential temperature (θ_v) values are collocated along the dryline (Ziegler et al. 1997). In that case the CBL deepening may create or intensify the trough along the dryline, thus enhancing the low-level convergence, and in particular increasing the inflow of moist air from the east (Ziegler and Hane 1993). Such moisture convergence and corresponding CBL deepening also increases the total-column precipitable water near the dryline and destabilizes the atmosphere (Wilson et al. 1992; Hane et al. 1993; Fig. 17 in Ziegler and Rasmussen 1998).

A horizontal θ_v gradient across the dryline has been revealed by airborne and ground-based measurements (Benjamin and Carlson 1986; Parsons et al. 1991; Ziegler and Hane 1993; Ziegler and Rasmussen 1998; Atkins et al. 1998; Demoz et al. 2006; Weiss et al. 2006) and modeling studies (Sun and Ogura 1979; Sun and

Corresponding author address: Bart Geerts, Department of Atmospheric Sciences, University of Wyoming, Laramie, WY 82071. E-mail: geerts@uwyo.edu

DOI: 10.1175/MWR3354.1

Wu 1992; Ziegler et al. 1995). The reported θ_v gradient is about 1–2 K over a distance of about 10 km. In all these studies the moist air (east of the dryline) has a higher density (lower θ_v) than the dry air. This horizontal gradient in θ_v drives a solenoidal circulation, with dry air rising over the moist air. This may contribute to finescale low-level convergence, thereby amplifying the humidity contrast and causing frontogenesis (Parsons et al. 1991; Sun and Wu 1992; Ziegler et al. 1995; Atkins et al. 1998). In some cases the θ_v gradient is sufficient for the moist air mass to propagate westward, with the leading edge (the dryline) assuming the characteristics of a density current (Parsons et al. 1991; Atkins et al. 1998). Numerical studies have confirmed this process (Ziegler et al. 1995; Shaw et al. 1997).

Substantial variations in the dryline horizontal structure, such as bulges, horizontal convective roll intersections, and misocyclones, can occur (e.g., Hane et al. 1997; Atkins et al. 1998), and they did on 19 June 2002 (Murphey et al. 2006, hereafter M06). The focus of this study is on the finescale variations in the vertical structure, especially with regard to CI.

The first objective of this case study is to describe the finescale kinematic and thermodynamic structure of a preconvective dryline in vertical cross sections. We focus on the echo and velocity structure as documented by an airborne cloud radar, and interpret these in the context of flight-level observations. The second objective is to demonstrate that the vertical tilt of the dryline echo, and the associated solenoidal circulation, were driven by a buoyancy difference, and to examine whether this circulation could have affected CI.

Data sources and processing are described in section 2. The larger-scale evolution is described in section 3. Section 4 describes the vertical structure and evolution of the dryline before CI. The relationship between kinematic and thermodynamic changes in the vicinity of dryline and its possible impact on CBL deepening and CI are addressed in the discussion.

2. Data sources and processing

As part of the 19 June mission in the International H_2O Project (IHOP_2002; Weckwerth et al. 2004), the University of Wyoming's King Air Aircraft (WKA) flew several transects across a nearly stationary dryline in NW Kansas, from 1900–2130 UTC, at elevations between 100 and 4000 m above ground level (AGL). The WKA flew stepped traverses, allowing for the examination of flight-level thermodynamic and wind measurements in vertical cross sections across the dryline. WKA data, with excellent horizontal resolution, are complemented with radiosonde data, with excellent vertical resolution, for those traverses that do have suitable soundings. Data from both aircraft dropsondes and ground-based balloon sondes were collected in very close proximity. Three mobile sounding systems of the Mobile Cross-Chain Loran Atmospheric Sounding System (MCLASS) GPS type (MGLASS) participated in the mission.

Along each flight leg the in situ data are interpreted in the context of millimeter-wave radar data, synchronized with WKA data at 25 Hz. The 95-GHz dual-channel Doppler Wyoming Cloud Radar (WCR; Pazmany et al. 1994) aboard the WKA operated mainly in profiling and vertical-plane dual-Doppler (VPDD) modes (Fig. 2 in Geerts et al. 2006). In the profiling mode, radar data portray the vertical structure of the CBL over its entire depth except for a ~220-m-deep blind zone centered at flight level (Geerts and Miao 2005a). The VPDD mode allows an estimation of the along-track 2D air circulation below the aircraft. The extraction of the echo motion from the Doppler velocity measured from a moving platform, and the dual-Doppler synthesis, are discussed in Damiani and Haimov (2006) and Leon et al. (2006). In a turbulent environment such as the CBL, the velocity uncertainty is about 1 m s^{-1} at ranges less than 2 km (Damiani and Haimov 2006). The WCR reflectivity profiles yield a rather accurate estimate of the local CBL depth, at least in fair-weather conditions (Miao et al. 2006). We use the Miao et al. (2006) algorithm to determine the CBL top from WCR reflectivity profiles (denoted as z_{i_WCR}). In essence this algorithm averages Z profiles over 10 s (800–850 m along track) and then identifies the region with the largest negative gradient in Z. The true (thermodynamic) CBL depth, denoted as $z_{i,\mathrm{th}}$, is the lowest level of a layer with sustained increase in potential temperature θ with height, inferred from soundings. Usually the water vapor mixing ratio (r_v) is well-mixed below $z_{i,\mathrm{th}}$. We also use the CBL depth estimates from the Mobile Integrated Profiling System (MIPS) 915-MHz wind profiler (Karan and Knupp 2006, hereafter KK06). Wind profilers most likely sense Bragg scattering in a region of rapid humidity decrease (Ecklund et al. 1988). This decrease can occur at $z_{i,\mathrm{th}}$, but soundings indicate that it may occur somewhat higher.

Many IHOP_2002 probes sampled the 19 June dryline (Weckwerth et al. 2004). This study further uses data from seven mobile mesonet (MM) vehicles and the third Doppler on Wheels (DOW3) X-band radar. The DOW3 0.5° or 0.6° elevation scan of reflectivity and velocity data plus simultaneous MM data are used in this study to provide a horizontal context for the WCR–WKA vertical-plane transects.

Of particular interest is the horizontal variation of θ_v: positive θ_v anomalies are buoyant, that is, they tend to

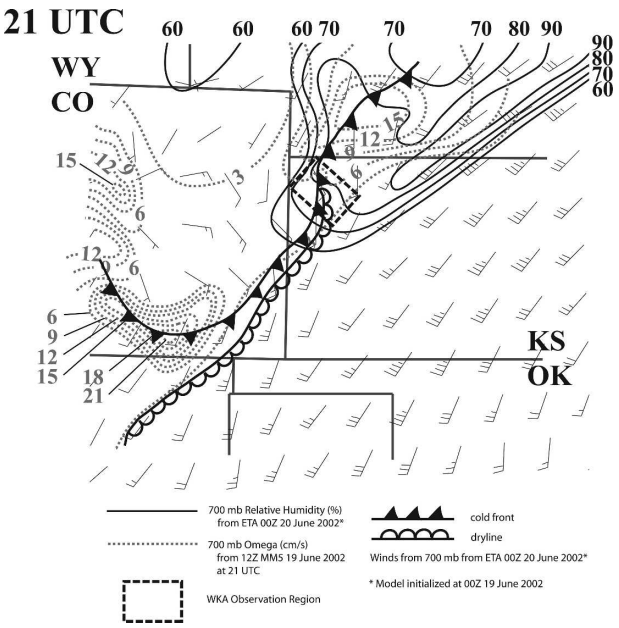

FIG. 1. Analysis of relative humidity, vertical air motion ("omega"), and winds at 700 hPa at 2100 UTC 19 Jun 2002, based on the 1200 UTC 12-km Location Analysis and Prediction System (LAPS) MM5 and Eta models. Only regions of upward motion are shown. A full barb is 10 kt. The cold front and dryline locations apply to ground level. Straight solid lines are state boundaries. The area of intensive observations is in NW KS, just south of the intersection between the cold front and dryline.

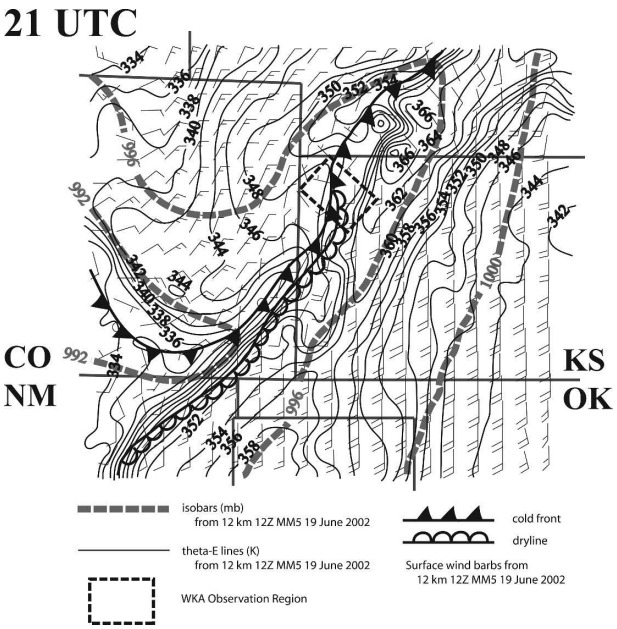

FIG. 2. Same as in Fig. 1, but showing sea level pressure, surface wind, and surface θ_e, based on the 1200 UTC 12-km LAPS MM5 model run.

rise spontaneously, at least if they are rather small scale (e.g., Houze 1993, p. 225; Doswell and Markowski 2004). Also, a horizontal θ_v gradient within the CBL, of sufficient strength to trigger a solenoidal circulation, leads to localized convergence, evident on radar as a fine line. In the presence of a mesoscale θ_v gradient, this convergence enhances the cross-boundary θ_v difference (i.e., it is frontogenetic), and this may lead to a density current, whereby the less dense air is forced over the denser air. Another key variable is equivalent potential temperature θ_e: air masses on either side of the dryline can be clearly contrasted in terms of θ_e, and θ_e values can be used to assess airmass mixing in the dryline convergence zone (DCZ). We also look for regions of anomalously high θ_e values within the CBL or at least below the level of free convection (LFC) since such anomalies imply anomalously low convective inhibition (CIN) for parcels originating at the level of the anomaly (e.g., Weckwerth et al. 1996; Crook 1996), and a deeper layer of potential instability.

3. Synoptic situation

The 19 June dryline was studied far north of the typical dryline occurrence, in NW Kansas. It developed as part of a weak frontal system (Fig. 1). An upper-level trough and a weak downstream jet maximum were present over North Dakota in the late afternoon, and the downstream ridge was situated from SW Texas into central Arkansas. Around 2100 UTC high relative humidity was found at 700 hPa as far south as NW Kansas. This humidity was associated with moderate lift and strong prefrontal southwesterly flow (Fig. 1).

A southerly low-level jet, about 15 m s^{-1} at 1900 UTC, was centered across west-central Kansas, ahead of the cold front. This jet advected moisture and contributed to high θ_e values locally exceeding 360 K at 2100 UTC (Fig. 2), in particular in NW Kansas, near a well-defined SW–NE-oriented wind shift line with northeasterly winds to the west and southerly winds to the east (Fig. 3). This line had the synoptic characteristics of a cold front, but the temperature gradient was weak: surface observations indicate a gradient of 8 K over a 100 km distance at 1100 UTC, dropping to 3 K (100 km)$^{-1}$ at 1800 UTC, and remaining steady toward 2100 UTC. The decrease in temperature contrast is apparent in Fig. 3. This frontolysis is assumed to be due to daytime differential boundary layer heating across the cold front.

Two soundings were launched on the moist side of the moisture gradient in northwest Kansas, in the morning of the 19 June 2002. These soundings reveal a rapid deepening of the mixed layer as evidenced by the change in height of the capping inversion. By 1647 UTC

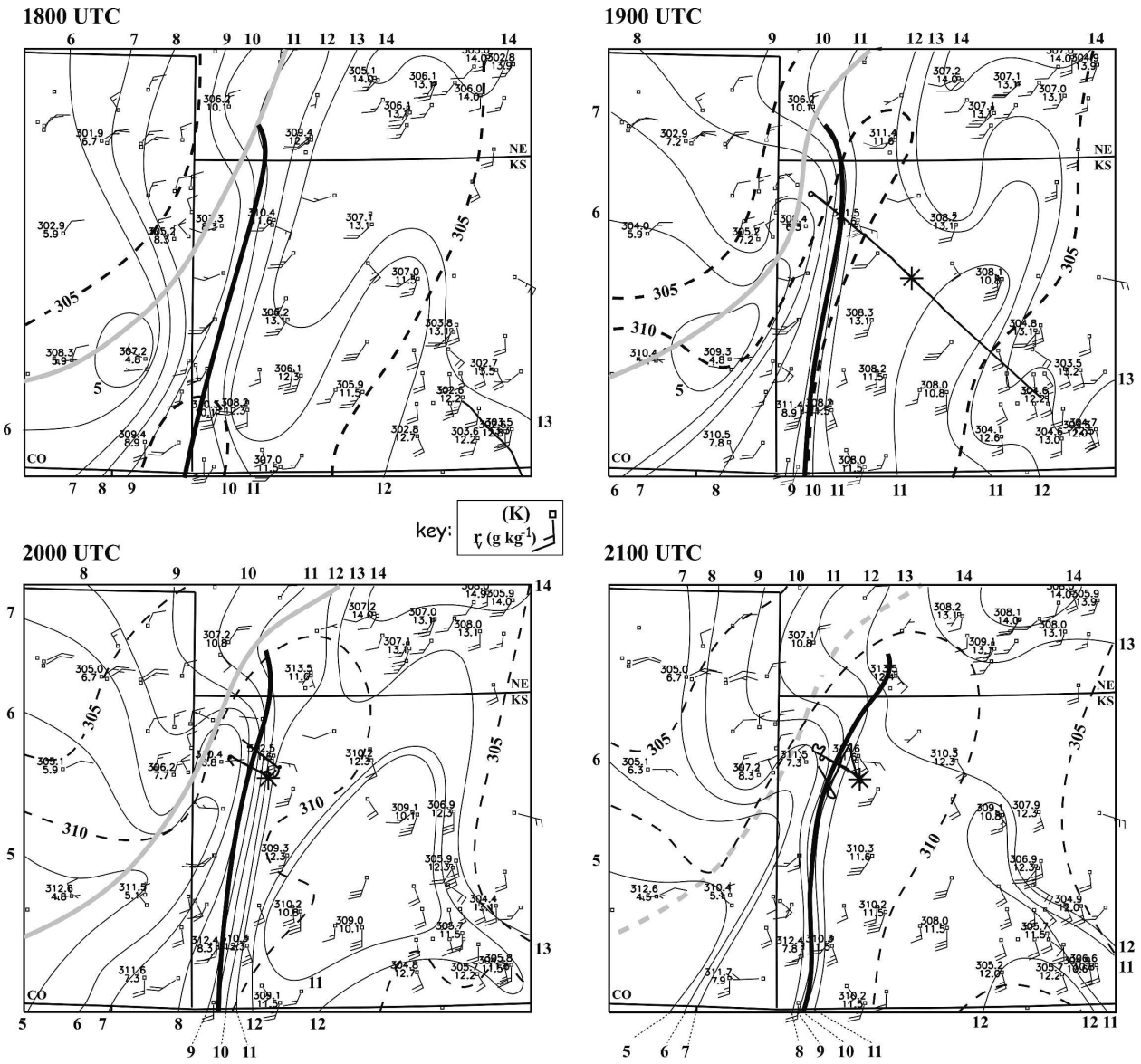

FIG. 3. Surface potential temperature and mixing ratio analysis for NW KS and surroundings at 1800, 1900, 2000, and 2100 UTC 19 Jun 2002. The dryline (cold front) is analyzed as a boldface black (gray) line. A 30-min flight track of the WKA, centered on the analysis time, is shown as a thin black line.

(2 h before local solar noon), the CBL was already 1200 m deep, with an average θ_e of 350 K. But the CBL was still well capped and the CIN totaled 464 J kg^{-1} (Table 1).

A wedge of low-θ_e air was advected from the southwest between the cold front and the developing dryline, just west of a broader region of high-θ_e air extending ahead of the cold front into Nebraska (Fig. 2). This wedge is apparent as a dry wedge in the surface data, especially at 2000 UTC (Fig. 3). Another region of high-θ_e air was advected into NE Colorado by the cyclonic low-level circulation. The low-θ_e wedge reached remarkably far north yet remained connected to its source region over New Mexico. The southeastern edge of this wedge is analyzed as a dryline. This dryline was sustained by confluent surface flow, and a large humidity gradient developed: surface dewpoints measured about 17°C in SW Kansas at 1800 UTC, with southerly flow at ~8 m s^{-1}, but only ~4°C in the dry wedge in SE Colorado and New Mexico with westerly to southwesterly flow at roughly 5 m s^{-1}. The 12-km fifth-generation Pennsylvania State University–National Center for Atmospheric Research (PSU–NCAR) Mesoscale Model (MM5) builds convective available potential energy

TABLE 1. Summary of soundings released in the vicinity of the dryline. Positive locations are on the east (moist) side, negative locations are on the dry (west) side, and the corresponding columns are set italic. The $z_{i,\mathrm{th}}$ is the CBL depth as inferred from the potential temperature (θ) profile: it is the base of the first stable layer above the mixed layer (specifically, $\Delta\theta \geq 1.0$ K over any depth, and θ does not decrease higher up). The "cap strength" is the θ increase in the stable layer above the CBL. This layer is defined as $d\theta/dz > 3$ K km^{-1}, and is at most 1 km deep. CAPE is not computed because several soundings do not reach the level of neutral buoyancy. Instead the temperature difference between parcel and environment ($T_p - T_e$) at 1 km above the LFC is shown. This difference is more relevant to CI. The mixed-layer averages in the last four rows are computed from the surface to $z_{i,\mathrm{th}}$.

Time (UTC)	1400	1647	2000	2002	*2018*	2040	*2057*	*2113*	*2119*	*2122*	2125	2141	2150
Location vis-à-vis dryline (km)	N/A	N/A	10	22	*−9*	2	*−11*	*−1*	*−27*	*−2*	23	−17	2
Sounding type	MCLASS	MGLASS	MGLASS	MCLASS	*MGLASS*	MGLASS	*MGLASS*	*MGLASS*	*Drop*	*Drop*	Drop	*M-Glass*	M-Glass
CIN (J kg^{-1})	−913	−464	−45	−130	*−132*	−19	*−130*	*−59*	*−108*	*−14*	−35	*−103*	−6
LCL (m AGL)	999	1973	3104	3020	*3679*	3640	*3920*	*3749*	*3840*	*3569*	2872	*3927*	3303
LFC (m AGL)	4895	4026	3172	3980	*4046*	3687	*4387*	*4035*	*4581*	*4021*	3468	*4115*	3303
LFC − LCL (m AGL)	3896	2053	68	960	*366*	48	*467*	*285*	*741*	*453*	595	*188*	0
$z_{i,\mathrm{th}}$ (m AGL)	304	1210	2243	2098	*1686*	2701	*2110*	*2698*	*1792*	*2967*	2070	*2243*	3480
Cap strength (K)	11.8	7.4	2.7	3.3	*2.8*	1.4	*2.7*	*1.3*	*2.6*	*1.6*	3.4	*1.9*	no cap
$T_p - T_e$ (K) at (LFC + 1 km)	1.8	5.4	5.1	5.3	*5.1*	5.5	*5.0*	*5.2*	*N/A*	*5.0*	5.4	*5.1*	4.8
Mixed-layer averages													
Potential temperature (K)	304	313	319	319	*320*	321	*320*	*321*	*319*	*320*	319	*320*	321
Mixing ratio (g kg^{-1})	12.3	11.8	9.3	8.7	*7.8*	8.5	*6.7*	*7.5*	*6.0*	*7.9*	10.5	*7.1*	6.5
Equivalent potential temperature (K)	341	349	346	343	*340*	347	*338*	*346*	*336*	*344*	351	*343*	343
Virtual potential temperature (K)	306	315	321	321	*321*	323	*321*	*322*	*321*	*321*	320	*322*	322

(CAPE) values up to 3500 J kg^{-1} at 2100 UTC, in the prefrontal high-θ_e wedge just north of the Kansas–Nebraska state line, near the θ_e maximum in Fig. 2 and the r_v maximum in Fig. 3. At the same time it erodes CIN to under 50 J kg^{-1} in the same belt but closer to the dryline/front, resulting in CI in the model in NW Kansas around 2130 UTC, 25–50 km east of the actual CI in that region. A region of lower CAPE values is found in the dry wedge, as well as behind the southern extent of the cold front.

4. Vertical structure of the dryline

a. The early phase of the dryline

Operational surface data show that the cold-frontal wind shift crossed the NW corner of Kansas around 1800 UTC (Fig. 3). The exact position of the cold front is somewhat uncertain, because it was not marked by a radar fine line, but a series of dropsondes, MM vehicles, and the Naval Research Laboratory WP-3D aircraft (M06), and all registered the wind shift and humidity increase characteristic of this weakening front. The lack of cold-frontal fine-line echo suggests that this front was not convergent.

Around 1900 UTC, a fine line became evident in the 0.5° elevation scan of the Goodland, Kansas, Weather Surveillance Radar-1988 Doppler (WSR-88D) radar and slowly propagated to the southeast. The DOW3 monitored this fine line beginning at 1930 UTC (Fig. 4). Electra Doppler Radar (ELDORA) dual-Doppler syntheses demonstrate air convergence near this line (M06). This line is traversed 11 times by the WKA between 1907 and 2138 UTC. Throughout this period a sharp r_v difference existed across this line, increasing from 1.1 to 1.9 g kg^{-1} over 10 km, according to WKA data along the lowest flight legs in the CBL. Hence it is referred to as a dryline. This dryline remained roughly parallel to the cold front, located 30–50 km to the nortwest (see Fig. 2 in M06). None of the WKA flight legs penetrated the cold front.

The WKA conducted the first of three stepped traverses across the dryline as soon as it developed (Fig. 5). WKA data from the four legs of this traverse are not advected relative to a central time in the stepped traverses, because the mean dryline speed (~3 m s^{-1} to the SE) is small compared to the differential flow normal to the dryline (i.e., the confluent wind component). Estimates of z_{i_WCR} (section 2) are available for all but the first flight leg, which was at about 1350 m AGL, slightly higher to the east because of the general terrain slope (Fig. 5a). In situ r_v and θ_e values indicate that this leg was dipping in and out of the CBL: drier air from above the CBL is intercepted several times along this flight leg (Fig. 5a), suggesting large local variations in the CBL depth ($z_{i,\mathrm{th}}$). The z_{i_WCR} estimates from subsequent lower flight legs indicate that the CBL was about 1700 m deep above the dryline and ~1400 m in the surrounding (Fig. 6), and was deepening with time.

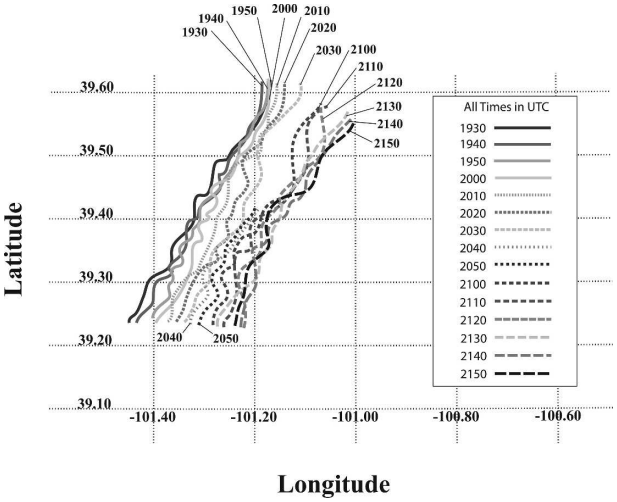

FIG. 4. Series of positions of the dryline fine line, inferred from DOW3 reflectivity data between 1930 and 2150 UTC.

The dryline boundary is apparent at each level of the stepped traverse. At the highest level, for instance, the r_v difference between the moist and dry air masses was 1.8 g kg^{-1}, and the θ_e difference was 4.8 K (Table 2). The dryline corresponded with a sharp r_v discontinuity (at 1918 UTC, line A in Fig. 5a). Such jump can only be maintained by convergent flow, which was present at low and middle levels in this stepped traverse (Table 2). Divergent flow was observed at the highest flight level (at ~1350 m AGL). The convergence from the three lowest flight legs, at a scale of ~10 km, implies a 10-km-wide updraft of 0.5 m s^{-1} near 1 km AGL. The convergence also implies moisture convergence: in the absence of vertical or along-line advection, Δr_v would approximately double in 1 h, at low levels (Table 2). Clearly much of this moisture was carried out again by the divergent flow in the upper CBL, but not all: KK06 document an increase of precipitable water in the DCZ between 2000 and 2030 UTC. The WKA data do not have the vertical resolution to compute vertically integrated moisture convergence, but a net water vapor increase over the depth of the CBL near the dryline is conceivable.

The distribution of θ_e in the first stepped traverse (Fig. 5) suggests that moist (dry) air was rising (sinking). This hypothesized circulation is consistent with the distribution of θ_v: the dry-side θ_v was 0.4–1.1 K lower than the moist-side θ_v in the two lowest flight legs

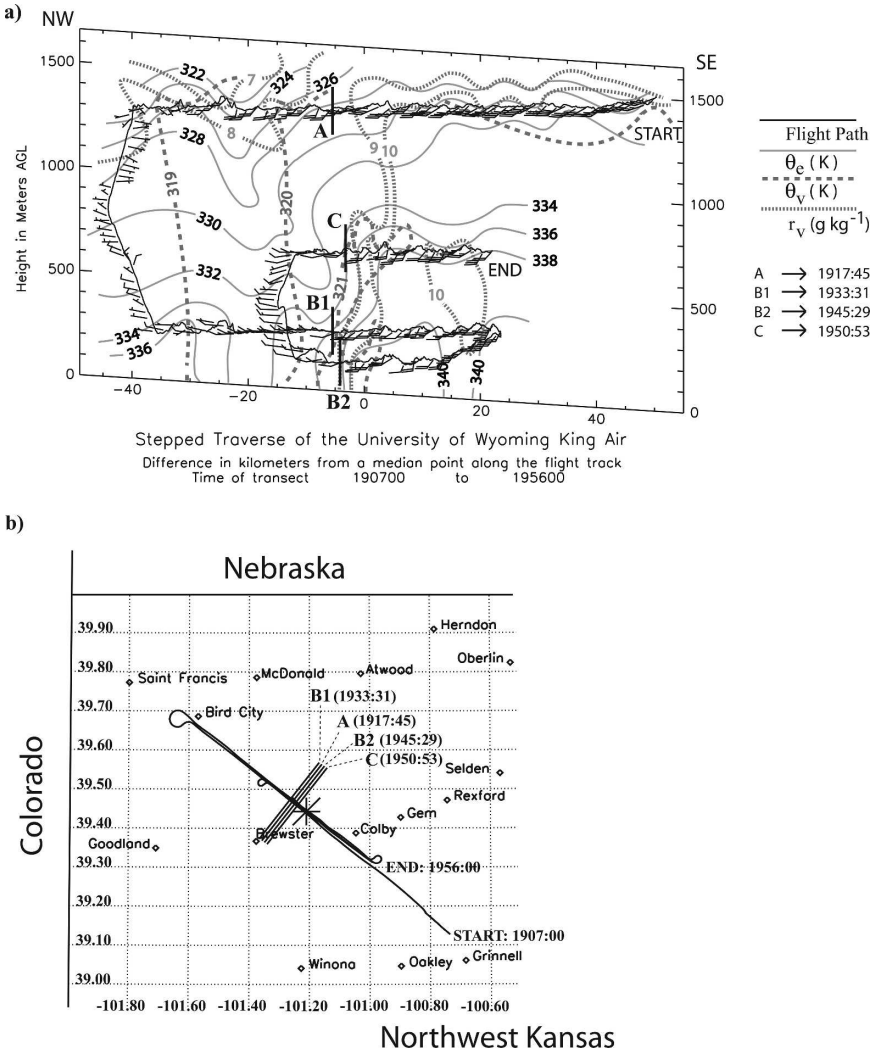

FIG. 5. (a) NW–SE cross section across the dryline based on WKA data collected between 1907 and 1956 UTC. The vertical solid lines indicate the location of the r_v jumps that mark the dryline. Wind barbs are taken from gust probe 1-Hz data and are plotted at a regular interval (full barb = 10 kt). Contours of θ_e, θ_v, and r_v are subjectively interpolated based on 10 s (≈850 m) average flight-level data. In this and all vertical transects in this paper, the moist (east) side is on the right. (b) Map of the corresponding WKA flight track. Some locations in northwest KS are also labeled. Track-normal solid lines denote the location and the time at which the dryline was intercepted by the WKA.

in this stepped traverse (Table 2). Changes in θ_v are far less sharp than those in r_v (shown below), and only become apparent when one averages over some distance (Table 2). Thus, unlike a density current, this dryline cannot be defined in terms of θ_v. Aside from the horizontal gradient of θ_v, there was a local θ_v maximum (~0.5 K above the background) within a ~1-km-wide zone around the dryline at all levels (Fig. 5). This implies that the near-dryline air was slightly buoyant relative to both adjacent air masses.

It should be mentioned that the stepped traverses such as shown in Fig. 5 do not reveal the large horizontal variability that has been documented along this dryline (M06). Misocyclones and associated updraft cores apparently traveled along the dryline with the mean southerly wind. Therefore it is not surprising that consecutive, geographically fixed flight legs reveal significant differences in cross-dryline flow, echo and updraft plume strength, and CBL depth. Yet the basic thermodynamic contrast across the dryline, as well as the vertical echo structure and secondary circulation, should remain the same.

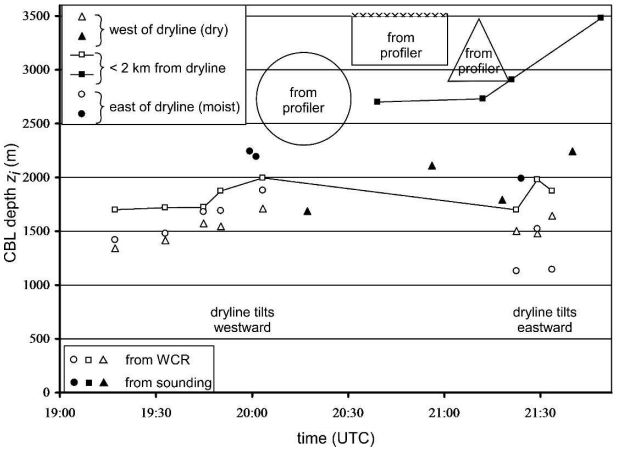

FIG. 6. Trend of CBL depth in the vicinity of the dryline, as estimated from WCR reflectivity profiles, from soundings, and from the MIPS 915-MHz wind profiler. Three regions are distinguished, one west (triangles), one east (circles), and one within 2 km of the dryline (squares). The latter are connected by a line, for clarity. The precise dryline location is based on a jump in WKA mixing ratio data and on DOW3 reflectivity maps. WCR data east and west of the dryline come from a 2-km-wide zone (2–4 km from the dryline), but soundings were released farther from the dryline, as far as 27 km to the east or west (Table 1). The open symbols are depths derived from the average height of WCR echo plumes z_{i_WCR}. All flight legs across the dryline and clearly below the CBL are used. The filled-in symbols are based on soundings ($z_{i,th}$), summarized in Table 1. The large symbols are based on 915-MHz profiler signal-to-noise ratio profiles shown in Fig. 5 in KK06; the symbol size represents both the sample duration (x axis) and the CBL depth variation (y axis). Profiler data were recorded only up to 3.6 km AGL. The stationary profiler sampled all three zones as the dryline passed through; the DCZ (rectangle) and the regions to the east (circle) and west (triangle) are all 5–6 km wide.

b. *Vertical structure of the dryline in the early phase*

Three VPDD syntheses of WCR velocities are shown in Fig. 7. The horizontal axis of the fine line was within ~5° normal to the WKA flight leg, so the synthesized WCR wind field in Fig. 7 captures the dryline-normal flow. The VPDD syntheses in Fig. 7 are all based on a 100×50 m^2 grid, and the displays share the same color key, so comparisons can be readily made. Because of the small-scale vortices in the dryline (M06), the actual speed of sections of the dryline and the ambient flow can vary around the mean dryline propagation speed. Thus, the mean wind has been removed in the flow patterns shown in Fig. 7, but this wind was generally small (<4 m s^{-1}). Some data thresholding was done prior to synthesis, based on the signal-to-noise ratio, but the resulting flow field is not filtered. The vectors become increasingly noisy with increasing range from the aircraft because errors due to aircraft attitude and nonsimultaneity of the two Doppler measurements increase with range (Damiani and Haimov 2006). Nevertheless the main currents relative to the dryline appear to be captured and are highlighted by means of objectively drawn streamlines in Fig. 7.

The first VPDD section reveals an upright echo plume extending upward to flight level (Fig. 7a), associated with a deep updraft near $x = 750$ m. This updraft carries high r_v values to flight level, and tilts slightly to the west just below flight level, where a ~0.5 g kg^{-1} r_v jump near $x = 400$ m indicates the dryline intercept. There is some suggestion of a westward-tilting solenoid (shown as a blue ellipse in Fig. 6a), not only in the streamlines, but also in the location of the strongest echoes, to the east of the solenoid at low levels, and farther west at upper levels. Yet a clearly sloping echo plume is not present yet. Subsidence prevails in the eastern sector (Fig. 7b).

The two low-level dryline intercepts (B1 and B2 in Fig. 5a) are detailed in Fig. 8. In both transects clear jumps in θ_e and r_v are present, on the order of 4.5 K and 1.3 g kg^{-1}, respectively. Such gradients can only be sustained by confluent flow and rising motion. An abrupt change in θ_v is not present (Figs. 8a,d), although on average the moist air mass is lighter (θ_v higher) than the dry air mass (Table 2). The first WCR transect (Fig. 8b) shows rising motion over a width of ~1 km, but the updraft is on the dry side of the dryline. The updraft strengthens and narrows with height. No clear tilt is evident in the echo plume (Fig. 8c). The echo "anvil" suggests that upper-level divergent motion occurs in both directions, notwithstanding an average background θ_v deficit of 1.1 K in the dry air (Table 2).

c. *Westward-tilting dryline phase*

Some 13 min later the echo plume is stronger, and a westward tilt has developed (Fig. 8f). The dryline echo plume is a few hundred meters higher than the surrounding plumes. The reflectivity increase is not just local (along the WKA track): DOW3 data (not shown) indicate an improved definition of the fine line. The r_v jump coincides with the leading edge of the rearward-tilted echo. Rising motion now takes place on the moist side, in a ~3-km-wide region east of the dryline. Sinking motion occurs just west of the dryline. There is another convective updraft near $x = 3000$ m (Fig. 8e), and the echo associated with this thermal also tilts westward (Fig. 8f). Thus, one, possibly two solenoidal vortices pointing out of the page (to the southwest) have developed. The horizontal component of this circulation is unknown for this flight leg; it is inferred from the echo dispersal. The vorticity and the echo tilt are con-

TABLE 2. Summary of differences across the dryline 2 h before CI, based on flight-level WKA observations. The differences are (moist side) minus (dry side), based on mean values on either side of the dryline. The mean values are calculated over varying distances, about 10 km on average but ranging between 2.4 and 38 km, depending on the flight leg length and the location of the boundary across the flight leg. The "time" listed is the time of dryline crossing. In the fifth column, a positive θ_v difference means that the dry-side air mass is denser. In the penultimate column, the "confluence" is the dryline-normal wind speed difference. The dryline orientation is assumed to be 20° clockwise from north. Positive values imply convergence across the dryline, negative is divergent. The moisture convergence (last column) is based on the mean r_v and dryline-normal wind. To express this as a local tendency of r_v (g kg^{-1} h^{-1}), a distance Δx of 20 km is assumed. Rows that are part of the first stepped traverse are in regular font, the second stepped traverse is in italic, and the third is in boldface.

Variable Units	Flight level m AGL	Time UTC	Δr_v g kg^{-1}	$\Delta\theta_v$ K	Confluence m s^{-1}	Moisture convergence g kg^{-1} h^{-1}
Low-level legs	~150	1945:29	1.4	0.43	5.8	8.7
	~250	1933:31	1.3	1.06	5.0	7.6
	~250	**2130:01**	**2.1**	**−0.88**	**9.4**	**13.9**
	~300	**2123:29**	**2.2**	**−0.40**	**8.5**	**11.3**
Midlevel legs	~700	1950:53	1.5	0.28	4.6	6.9
	~900	*2004:02*	*2.3*	*0.34*	*1.6*	*2.4*
	~750	**2134:37**	**1.3**	**−0.60**	**6.1**	**7.6**
Legs in the upper CBL or above CBL	~1350	1917:45	1.8	0.04	−3.3	−5.2
	~1350	*2015:03*	*2.1*	*0.22*	*−4.6*	*−7.1*
	~1700	*2023:30*	*2.3*	*0.05*	*−4.7*	*−6.9*
	~3200	**2104:02**	**1.2**	**0.15**	**−2.1**	**−1.8**

sistent with the horizontal θ_v gradient (Table 2). It should be noted that the change in the vertical structure of the dryline, shown in Fig. 8, may be due to along-line variability (M06), rather than to temporal evolution.

A cross section across the dryline collected 6 min later (1951 UTC; line C in Fig. 5a) indicate that the dryline again is tilted toward the dry side (Fig. 9a), and that a vertical velocity dipole exists (Fig. 9b), although in this case both dry and moist air rise through the flight level. The updraft is ~1 km wide, deep, and strong (peaking at 9 m s^{-1}; Fig. 9b). This updraft is consistent with the strong confluence of the horizontal wind (Table 2) and with positive buoyancy at flight level ($\Delta\theta_v \sim 0.5$ K; Fig. 9c). We are referring to flight-level observations (~700 m AGL); larger differences can be expected at lower levels. The downdraft just west of the dryline (only partially shown in Fig. 9b) is about 2 km wide, and weaker. As a result, the dryline echo plume reaches up to ~1900 m AGL (Fig. 9a), which is higher than any plume along this flight leg (Fig. 6). On a larger scale, the dry side is slightly denser than the moist side even at this level, $\Delta\theta_v \sim 0.3$ K (Table 2), which is consistent with the dryline plume slope (Figs. 9a,d).

Between 2000 and 2030 UTC, a broken line of shallow cumulus began to develop along the radar fine line. A time series of DOW3 reflectivity images reveals a slowing southeasterly progression of the fine line (Fig. 4). The line also became thinner, more confluent, and better defined in terms of a higher peak reflectivity.

During this period a second WKA stepped traverse was flown (Fig. 10). It lacks low-level flight legs but is supplemented with sounding data. Soundings are rich in vertical structure information and thus complement flight-level data, which are rich in horizontal structure information. Several observations can be made. The averaged r_v contrast between moist and dry air masses increased, from 1.3–1.8 g kg^{-1} in the first stepped traverse to 2.1–2.3 g kg^{-1} in the second (Table 2). This appears mainly due to gradual drying west of the dryline, by ~1 g kg^{-1} in less than 1 h: compare r_v contour values in Figs. 10a and 5a. This is evidence for stronger entrainment of free-tropospheric air and CBL deepening on the dry side. In contrast, r_v changed little on the moist side.

WCR zenith antenna data were collected on one of the three flight legs in the second stepped traverse. These data, at 2004 UTC, suggest that the CBL top near the dryline was around 2000 m AGL (Fig. 9d), that is, higher than during the first stepped traverse. In addition echo plumes on the moist side continued to reach higher than on the dry side (Fig. 6). The dryline echo plume tilted westward, consistent with the θ_v gradient (Fig. 9f). A solenoidal circulation can be seen (Fig. 9e), with a strong downdraft on the west side and an updraft on the east side. This updraft is even stronger than the one at 1951 UTC (Fig. 9b), and is buoyant at flight level. Again moist and dry air sources mixed in the updraft.

During the second stepped traverse the averaged "air mass" $\Delta\theta_v$ remained positive (moist side less dense than the dry side). The $\Delta\theta_v$ values listed in Table 2 are smaller on average than during the first traverse, but

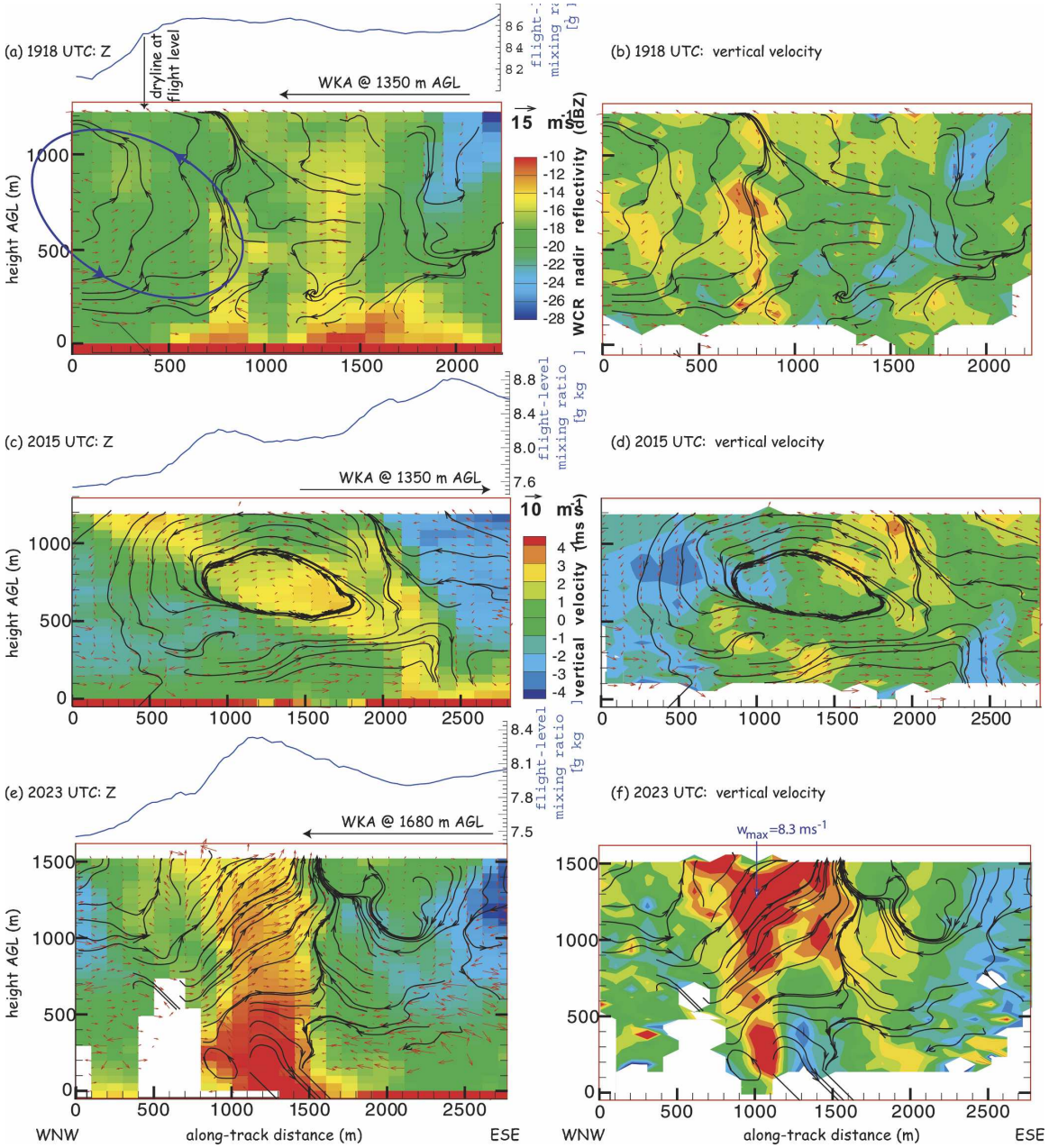

FIG. 7. (a), (b) Two-dimensional wind vectors inferred from WCR VPDD synthesis around 1918 UTC, for transect A in Fig. 5a. The aspect ratio (height:width) for this and all WCR transects in this paper is 1:1. The dual-Doppler grid resolution is 100 m in the horizontal and 50 m in the vertical. Thin black lines are select streamlines, i.e., tangent to the vectors. The large black arrow on top of (a) and in other WCR transects in this paper defines the path of the WKA. The horizontal flow shown is relative to the mean (-0.67 m s^{-1}, i.e., from right to left) in this cross section. The color field is WCR reflectivity in (a) and vertical velocity in (b). The blue ellipse in (a) schematically illustrates the inferred solenoidal circulation. A trace of flight-level r_v values is shown on top of (a). (c), (d) Same as in (a), (b), but at 2015 UTC, corresponding with line B in Fig. 10a. (A mean flow of $+3.51$ m s^{-1} from left to right has been removed.) (e), (f) Same as in (a), (b), but at 2023 UTC, corresponding with line C in Fig. 10a. (A mean flow of $+2.79$ m s^{-1} has been removed.)

that may be due to altitude: $\Delta\theta_v$ remains about the same for matching flight levels. At all levels in the second stepped traverse, θ_v was highest in the DCZ, compared to the ambient air masses on either side (Fig. 10a), by 0.5–1.0 K. Such buoyancy can drive rising motion and convergence near the dryline. It is unknown whether the low-level airmass confluence has changed in this stepped traverse. We do know that upper-level diffluence has become slightly stronger (Table 2).

A VPDD transect at 2015 UTC captures a clear,

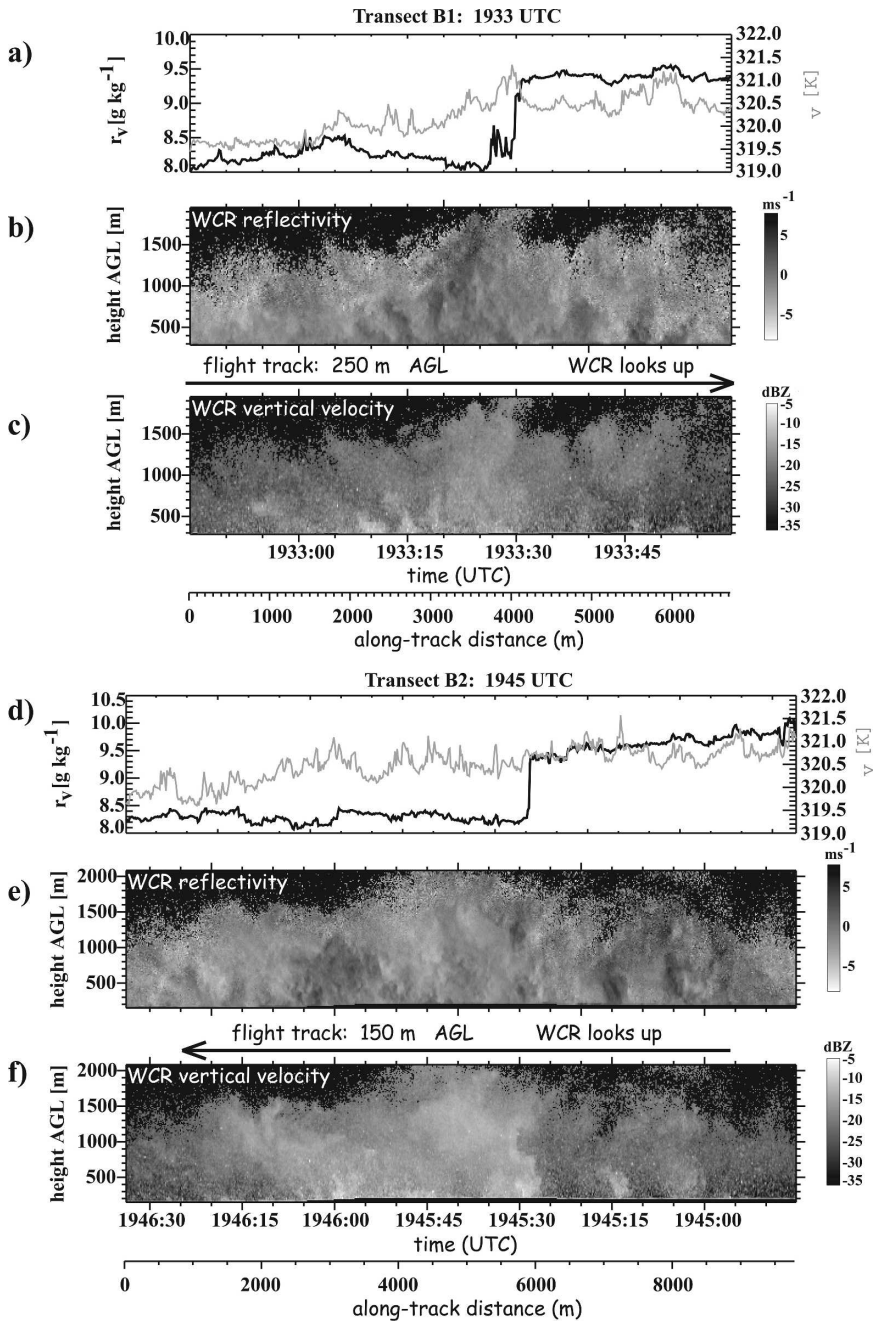

FIG. 8. WKA and upward-looking WCR data around (a)–(c) 1933 and (d)–(f) 1945 UTC. (a), (d) Flight-level mixing ratio and θ_v; (b), (e) WCR vertical velocity; and (c), (f) WCR reflectivity. Both the time (UTC) and along-track distance (m) are noted at the bottom.

2-km-wide solenoid with vorticity pointing south (Fig. 7c), associated with a clear echo plume tilt and a vertical velocity dipole peaking near 1 km AGL (Fig. 7d). This solenoid registered as a 3.4-km-wide, slightly buoyant (~0.1 K) updraft at flight level, averaging 2.0 m s^{-1} in strength. This updraft peaks just below flight level (Fig. 7d), leading to divergence at flight level (Table 2).

The 2023 UTC dryline passage is quite different: a more erect updraft and coincident strong echo plume from the surface to flight level (1680 m AGL; Fig. 7e). The updraft is narrow at its base, with a peak velocity of 6.5 m s^{-1} at a scale of 100 m at 300 m AGL, and broadens with height, suggestive of an entraining jet (Squires and Turner 1962). The maximum WCR updraft on the 100 × 50 m^2 grid (near 1300 m AGL in

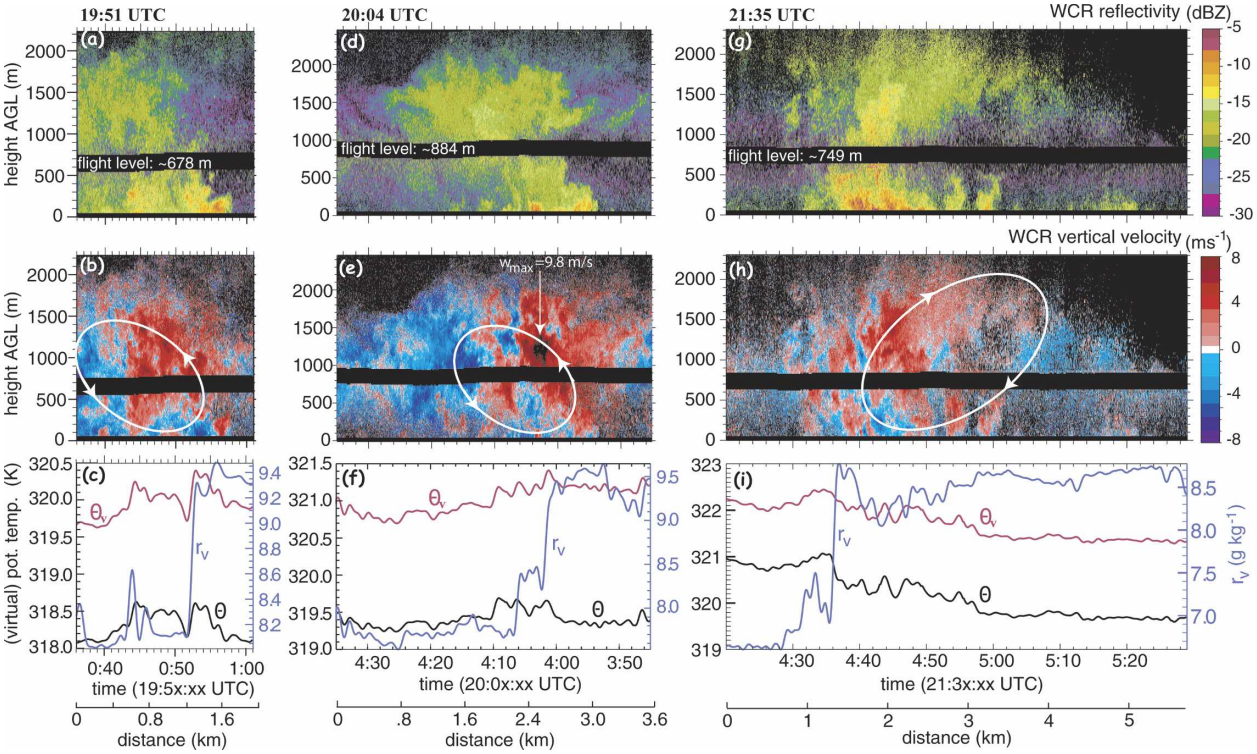

FIG. 9. (a), (d), (g) WCR reflectivity; (b), (e), (h) WCR vertical velocity; and (c), (f), (i) flight-level data. All flight legs are at midlevel (Table 2). Three dryline crossing are shown: (a)–(c) at 1951 UTC (leg C in Fig. 5a), (d)–(f) at 2004 UTC (leg A in Fig. 10a), and (g)–(i) at 2135 UTC (leg C in Fig. 12a). All WCR transects have a 1:1 aspect ratio and have the moist (east) side on the right. However, (a)–(c) are not wider because of WCR problems farther west.

Fig. 7f) is more than twice as strong as in the previous two transects (Figs. 7b,d). At flight level the gust probe measures a peak updraft of 10.6 m s^{-1}, apparently supported by a ~500-m-wide buoyant core with θ'_v ~ 0.8 K. DOW3 data at this time (not shown) show that the WKA crosses a dryline reflectivity core with cyclonic circulation, in other words the WKA appears to slice a misocyclone with a strong, deep updraft (Fig. 7f). The air rising through the echo plume from the west in Fig. 7e is actually moist air, as evident in the r_v trace, presumably wrapped around by the misocyclone. The VPDD circulation reveals deep confluent flow. The change structure from 2015 to 2023 UTC (Figs. 7c,e) probably is due to along-line variability, rather than a change in low-level horizontal θ_v gradient.

d. Erosion of convective inhibition

Two soundings released at 2000 and 2002 UTC (not shown) indicate that just east of the dryline the CBL was ~2200 m deep and the cap strength (defined in the caption for Table 1) was only ~3 K, resulting in small CIN values. Mean values of θ_e and r_v within the CBL decreased compared to the 1647 UTC sounding (Table 1), because of mixing with the dry free troposphere. These values were higher in the 2000 UTC sounding, which was closer to the dryline than the 2002 UTC sounding (Table 1). At 2000 UTC the lifting condensation level (LCL) came within 100 m of the LFC, suggesting that CI was imminent. A third sounding launched at 2018 UTC on the dry side had higher CIN and a lower CBL height compared with the moist side.

A fourth sounding released at 2040 UTC within the DCZ (~1.5 km on the moist side) reveals a near-zero CIN value and the near-collocation of the LCL and the LFC. In addition θ_e was higher compared to previous soundings (Table 1). Later soundings shown in Table 1 suggest that θ_e was also higher in the DCZ than in the surrounding area. At the same time the CBL was remarkably deep, yet the high θ_e values preclude much entrainment of free-tropospheric air, which had θ_e values ~20 K lower. We assume that less entrainment of free-tropospheric air occurred in the DCZ, compared to the vicinity, especially the dry side, and thus high r_v and θ_e values were sustained in the DCZ. Thus, the CBL deepening in the DCZ was not the result of surface fluxes and entrainment near z_i, but rather sustained convergence.

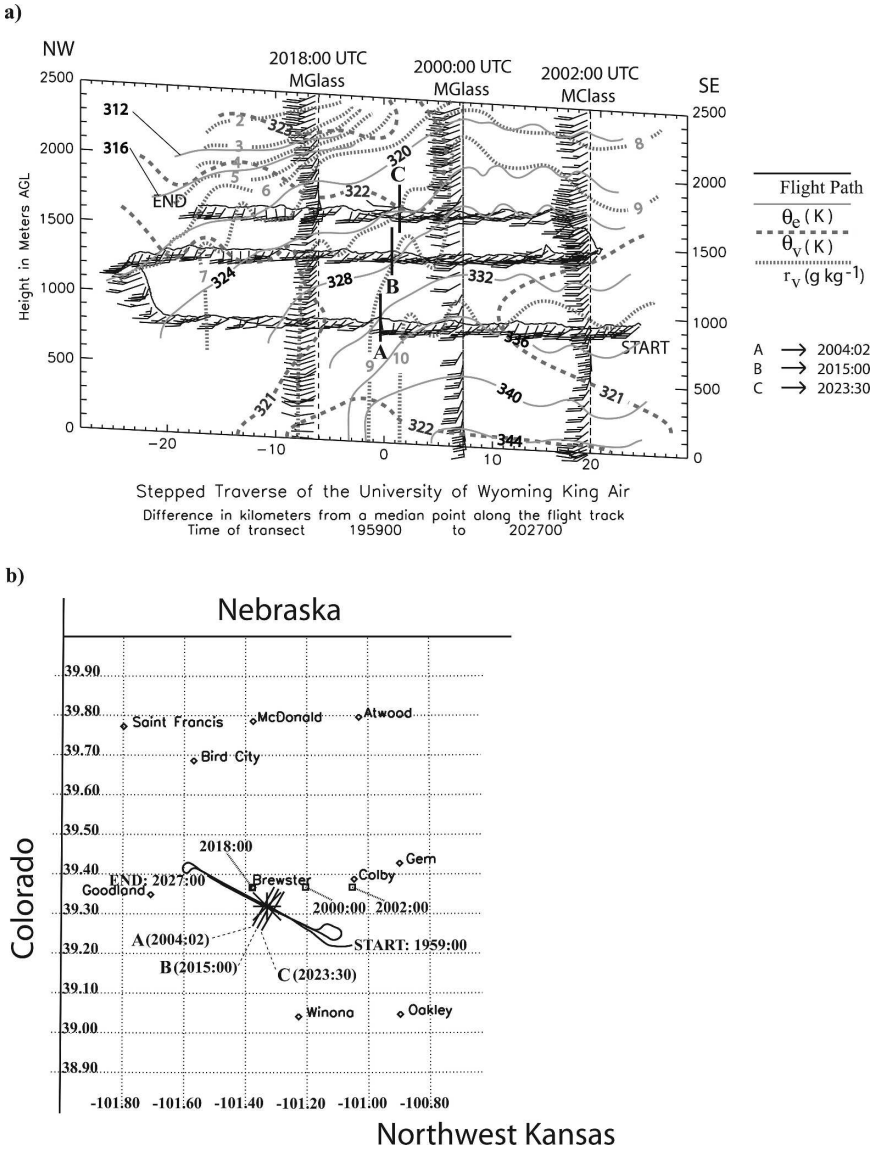

FIG. 10. Same as in Fig. 5, but for a stepped traverse between 1959 and 2027 UTC. (a) Three proximity soundings are included in the subjective interpolation. Their release time is shown on top, and their ascent is traced with wind barbs, plotted at a regular interval. (b) Their release location is shown, together with the WKA flight track.

In all these soundings, and especially in the 2040 UTC sounding, the lapse rate above the LFC was close to dry adiabatic at least in the first kilometer. This maximizes $(T_p - T_e)$ at LFC + 1 km (defined in Table 1) to 5.0–5.5 K and facilitates CI. The local atmosphere appeared ready for CI by 2040 UTC. It did not happen, but deep convection had already emerged along the dryline as far north as the Colorado–Kansas border. Soundings indicate that during the next hour, the near-dryline CIN increased slightly before dwindling toward zero (Table 1).

Around 2100 UTC the WKA flew at high altitude (~3.2 km AGL). The intent of this flight leg, in part along the same track as other flight legs, was merely to rest and cool the WCR. According to flight-level r_v and θ_e values along this leg, the CBL generally remained below 3.2 km AGL, although the MIPS 915-MHz profiler (KK06) recorded enhanced Bragg scattering around this level (Fig. 6). The WKA did encounter one rising, noncloudy plume about 4.5 km wide with thermodynamic properties of the CBL along this flight leg, at 2104 UTC, which positions the plume precisely above the dryline. (The dryline location was inferred from DOW3 reflectivity; an r_v jump that marks the

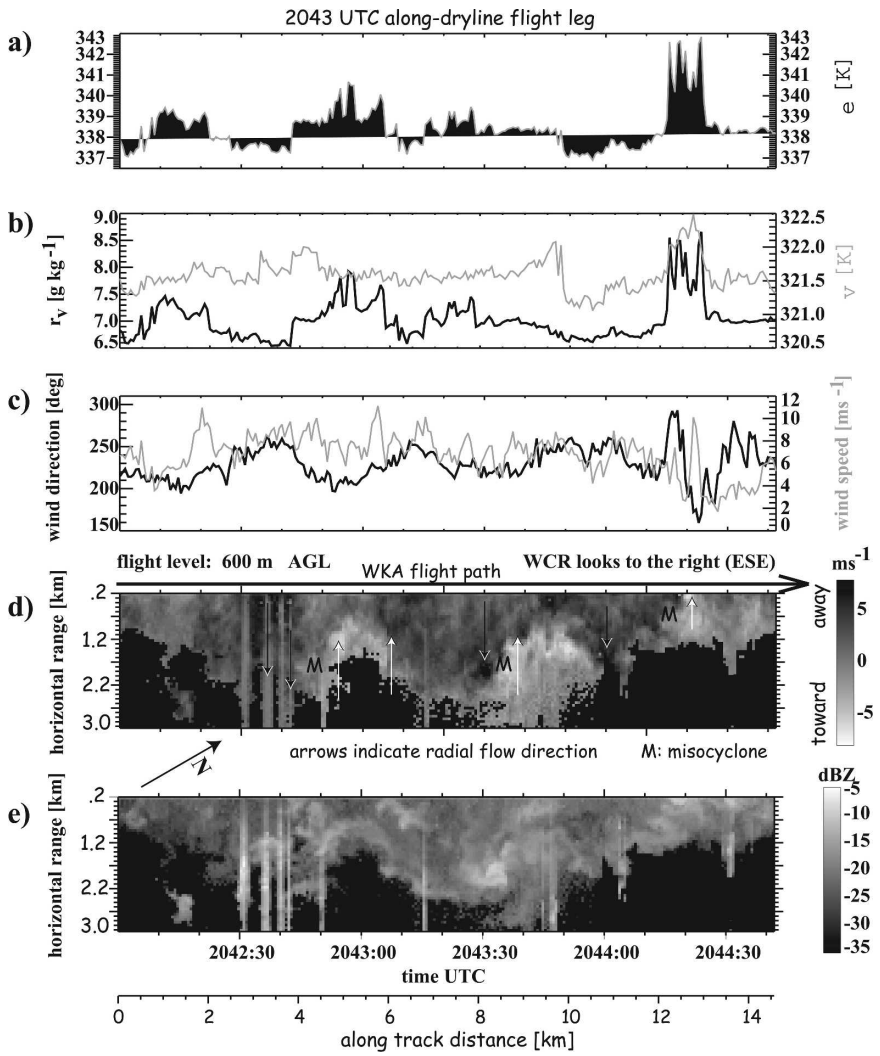

FIG. 11. WKA and side-looking WCR data around 2043 UTC: (a) θ_e, (b) r_v and θ_v, (c) wind direction and magnitude, (d) WCR radial velocity, and (e) WCR reflectivity. Both the time and along-track distance with respect to the left edge are noted at the bottom. The WKA flies at the top side of (d) and (e), from SSW to NNE, and the WCR antenna points to the right. Thus, the aircraft is mostly on the dry side and the WCR points to the moist side of the dryline.

dryline at low levels was not present at this level.) Within this plume θ_e peaked at 343 K and r_v at 8.5 g kg^{-1}. Surprisingly, the plume θ_v was about 0.6 K lower than in the surroundings. This suggests that the plume had overshot into the layer containing the little CIN that remained. The 2113 UTC sounding suggests that near the dryline the CIN layer (between z_i and the LFC) occurred between 2.7 and 4.0 km (Table 1). Thus, this plume was intercepted about halfway up in the CIN layer.

e. Close-up of the horizontal structure of the preconvective dryline

The dryline was quite contorted on small scales: ground-based and airborne X-band radar data show that cyclonic horizontal shear was concentrated and stretched in updrafts, yielding locally high vertical vorticity values (M06). The WKA flew one boundary-parallel leg at roughly 600 m AGL, mostly in the dry air just west of the dryline (Fig. 11). The dryline was highly contorted (Fig. 11e), yet strong confluence occurred toward this line (Fig. 11d). The flow even accelerated toward the boundary. At 2044:20 UTC the WKA briefly sampled the moist air, evident in the θ_e spike (Fig. 11a) and strong southerly flow (Fig. 11c), comparable in speed and direction to moist-side winds (Fig. 10a). This point coincides with a spike in θ_v (Fig. 11b). Does this higher θ_v imply that the dry air was still denser around 2044 UTC (supporting a tilted solenoi-

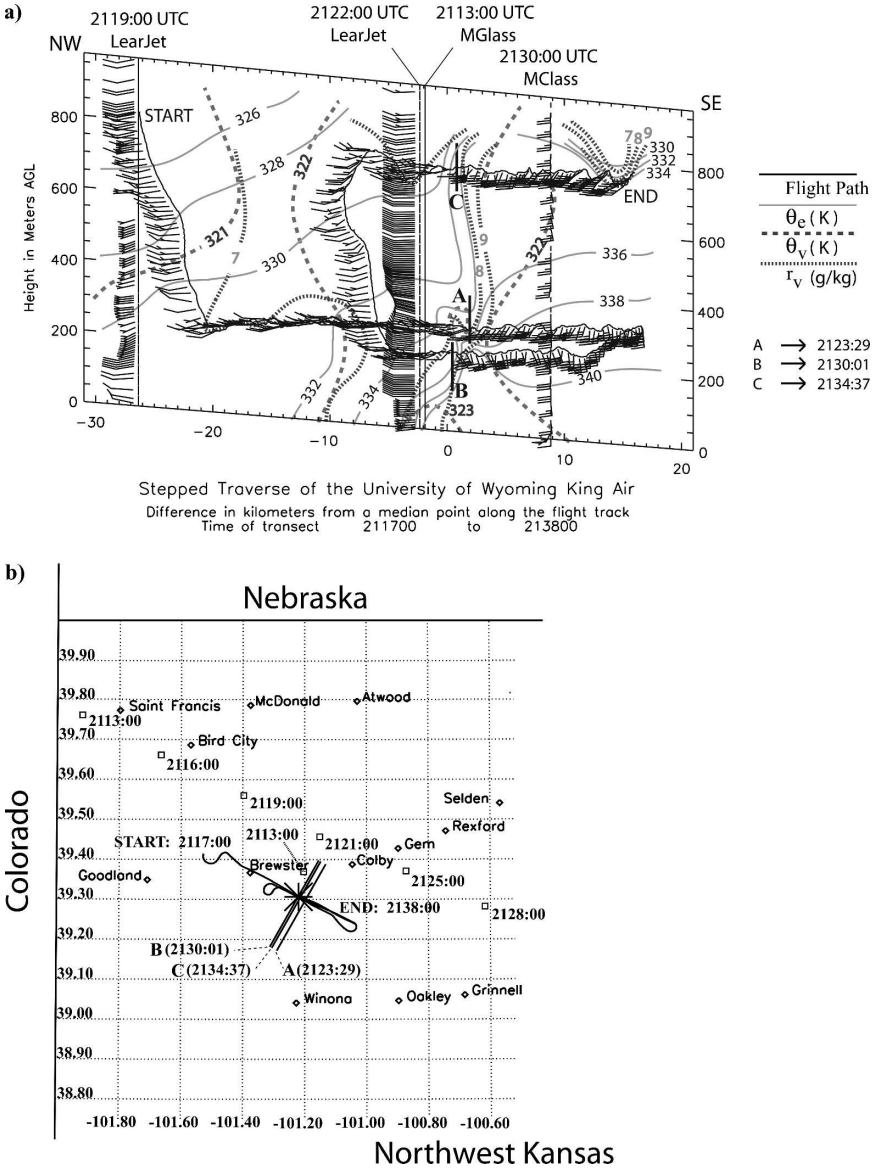

FIG. 12. Same as in Fig. 5, but based on three WKA flight legs between 2117 and 2138 UTC. (a) Profile data from three dropsondes and one upsonde are included. (b) The track of the Learjet dropsonde aircraft is evident from the dropsonde locations (squares).

dal circulation)? Or does it represent a local buoyant plume? The latter is likely since it is consistent with the higher reflectivity (Fig. 11e) and the 8 m s^{-1} flight-level updraft (not shown).

Clearly the dryline was a cyclonic shear boundary, and convective updrafts drawn toward the line spun up this horizontal shear in cyclonic patches (Wilson et al. 1992). The presence of misocyclones, such as the one shown in Fig. 11d at 2043:35 UTC and those shown in Fig. 8b in M06 at about the same time, is evident also in the spiral arms around echo cores (Fig. 11e), and in the dust devils reported by the mobile mesonet crew. Misocyclones may be important in CI (Wilson et al. 1992; Fig. 20 in M06) since they tend to coincide with sustained updrafts (Fig. 15 in Arnott et al. 2006) and thus greater CBL depths along the shear line, in this case a dryline.

f. Transition to the eastward-tilting phase

The fine line became quasi stationary between 2100 and 2150 UTC (Fig. 4), and moved westward after 2150 UTC. The CI occurred during the third and last WKA stepped traverse, mostly at low levels, between 2059 and 2138 UTC (Fig. 12). The dryline r_v contrast and

wind shift remained well defined during this period. As was the case in the previous two stepped traverses, the air within a kilometer from the dryline was buoyant ($\Delta\theta_v \sim 0.5$ K) relative to surrounding air, at all three flight levels shown in Fig. 12.

A remarkable transformation from a westward-tilting fine line, with denser air on the dry side, to an eastward-tilting line, with denser air on the moist side, occurred between about 2015 (Fig. 7c) and 2130 UTC (Fig. 13f).

The 2123 UTC transect (line A in Fig. 12a) is rather complex but already shows the transformation: a buoyant, eastward-tilting plume is intercepted at $x = 4500$ m (Fig. 13c) and is followed, farther east, by moist air of decreasing θ_v (see Table 2). Even though this plume does not dominate the cross section (Fig. 13c), it marks the dryline, since it is the location of maximum sustained r_v change (Fig. 13a). It is associated with a strong updraft (Fig. 13b) that lifts dry air over the denser moist air. About 1.5 km to the west (centered near $x = 3000$ m), a broader plume of higher reflectivity is found. It is a moist, buoyant eddy (Fig. 13a), ascending over the entire depth of the CBL at up to 8 m s^{-1} (Fig. 13b). One can speculate that the dry air between the two plumes represents a local vertical dry intrusion (Hane et al. 2001; Ziegler et al. 1995), yet there is little subsidence in this dry pocket (Fig. 13b). Wind observations at flight level (Figs. 13a,b) suggest that this eddy wrapped around counterclockwise from the moist side, as a result of a ~1.5-km-wide misocyclone. An annulus-shaped reflectivity structure and cyclonic wind shear are evident in DOW3 data at this location and time (Fig. 14). The core of this vortex (more evident after removal of the mean translation vector, shown as the "wind anomaly" in Fig. 13) contains dry air.

Some 7 min later (2130 UTC; line B in Fig. 12a), this vortex had advected to the north, out of the WKA transect. The WKA encountered a single wind shift line collocated with a 2 g kg^{-1} r_v jump (Fig. 13d), in fact at the same geographic location as 7 min earlier. The dryline plume clearly tilted eastward, and an echo anvil stretched east of the dryline (Fig. 13f) Thus, the echo plume and updraft in the 2130 UTC transect correspond with the smaller eastern plume in the 2123 UTC transect. The updraft had become a bit wider, but its slope and peak value (~7 m s^{-1}) was about the same as 7 min earlier.

The two low-level flight legs (Fig. 13) reveal confluence toward the dryline about twice as large as observed before, at 1933 and 1945 UTC (Table 2), due to stronger southerly flow (~14 m s^{-1} on the moist side), meeting ~6 m s^{-1} flow from ~240° on the dry side. As a result, low-level moisture convergence too was much larger than nearly 2 h earlier (Table 2).

At this time the θ_v gradient clearly had reversed (Fig. 13d). The moist-side θ_v was on average 0.9 K lower than the dry-side θ_v (Table 2). The vertical velocity dipole (Fig. 13e) also had reversed, consistent with the changed slope. It is indicative of a solenoidal circulation with vorticity pointing into the page (to the northeast). The center of this circulation was well on the moist side (Figs. 13d,e), such that moist air was lifted.

The dryline became quasi stationary around this time (Fig. 4), and some 20 min later (after 2150 UTC) the dryline started to propagate westward at an increasing speed. The slowing and later westward propagation may be explained by an increasing $\Delta\theta_v$ and density current dynamics. The ground-relative speed of a density current is affected by the ambient low-level winds (e.g., Simpson and Britter 1980). These winds blew the dryline to the (south)east at 1–4 m s^{-1}, according to two soundings just west of the dryline (Fig. 15), that is, a developing density current would have encountered a weak headwind.

g. *Convective initiation*

The WKA had one final encounter of the dryline at 2135 UTC (line C in Fig. 12) at ~750 m AGL, during which deep convection was in progress within the DOW3 domain. Specifically, the WCR recorded rain echoes reaching the ground at 2137 UTC at a location 9–15 km east of the dryline. Rain was obvious from the characteristic high reflectivity, downward motion, and an echo foot near the ground. DOW3 reflectivity animations suggest that this rain fell from a cell that developed at least 10 km to the south of the WKA transects. Later on larger cells developed and advected into the DOW3 domain, all east of the dryline, which accelerated westward.

In the final WKA transect, the moist side was clearly denser again (Fig. 9i) with a θ_v deficit of 0.6 K, and the mean confluence again was far higher than observed before at midlevels (Table 2). The echo plume tilted eastward and had an anvil (Fig. 9g). This plume contained several small up- and downdrafts at low levels (Fig. 9h), possibly indicating turbulence around a developing density current head. At flight level the updraft cores again lifted moist, cooler air. At higher levels a broad, less turbulent updraft occurs, trailed by a region of deep subsidence (4 km $< x <$ 5 km in Fig. 9h).

A series of dropsondes was released at about 22-km intervals during the third WKA traverse along a track roughly parallel to that of the WKA (Fig. 12b). This dropsonde transect provides a larger context of the environment, including the cold front, the dry wedge, and

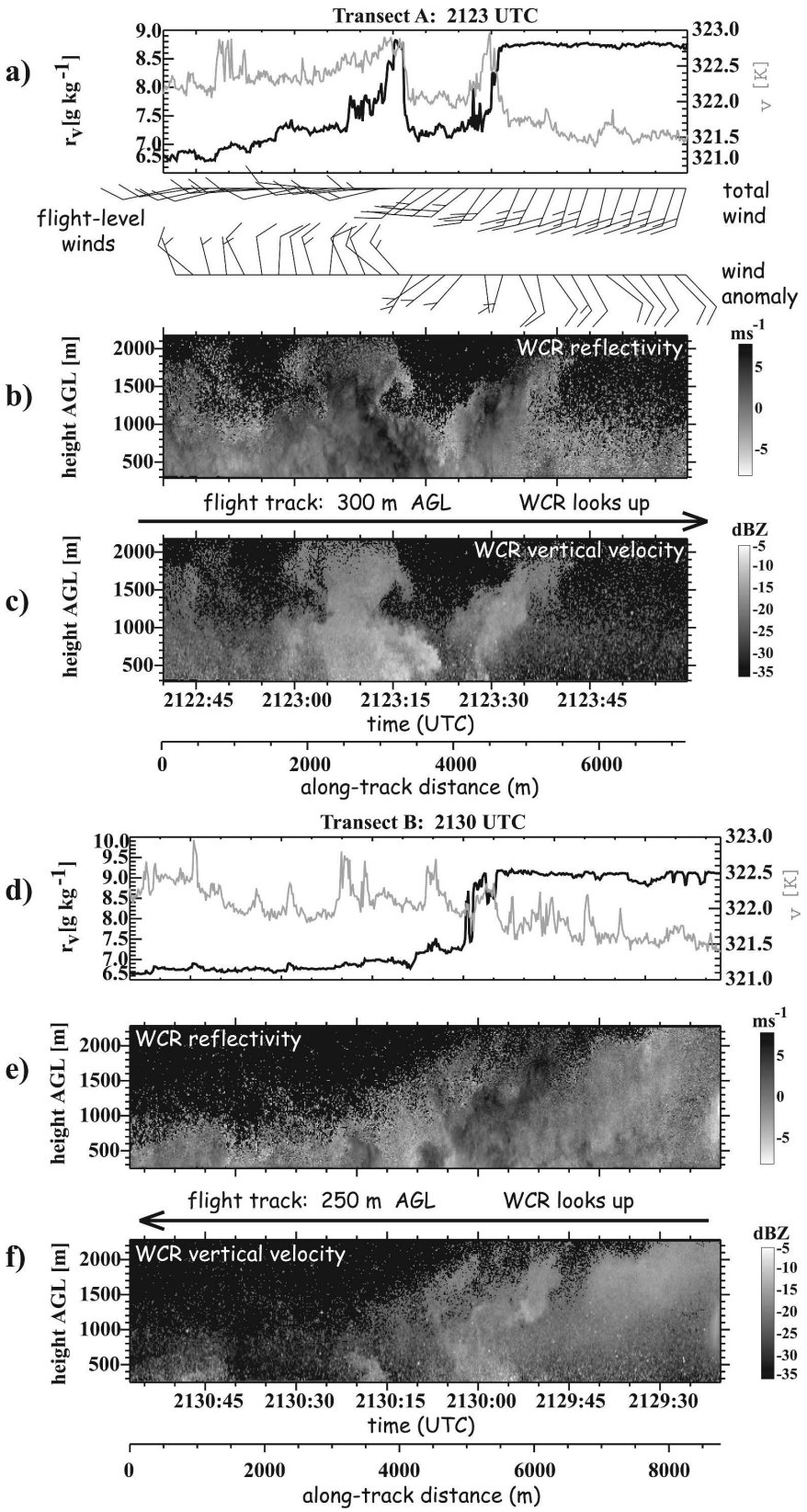

FIG. 13. Same as in Fig. 8, but for (a)–(c) 2123 and (d)–(f) 2130 UTC. Gust-probe wind barbs are shown for the 2123 UTC transect. The "wind anomaly" is the total wind minus the flight-leg-mean wind.

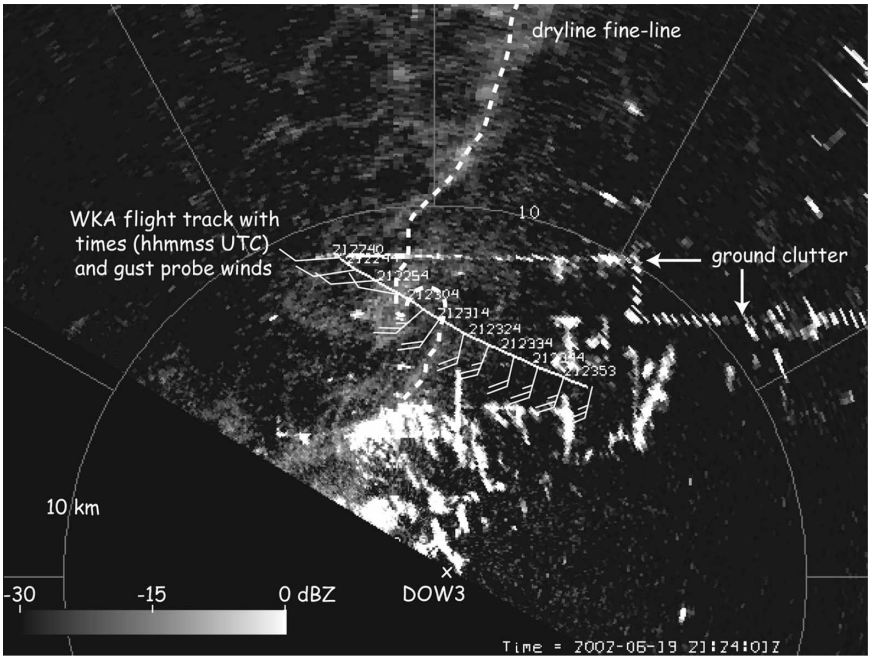

FIG. 14. DOW3 reflectivity at 2124 UTC plus WKA flight track and flight-level (300 m AGL) winds. A WCR vertical transect along this flight leg is shown in Fig. 13.

the dryline, just prior to CI (Fig. 16). The westward-sloping cold-frontal surface is evident in terms of a wind shift and a lower θ_v. In the moist air mass, $z_{i,\mathrm{th}}$ is clearly marked in terms of a rapid θ_e lapse. In the dry wedge and above the dryline, $z_{i,\mathrm{th}}$ is less well defined. The CBL was about 3000 m deep in the 2122 UTC sounding, higher than in any other previous sounding (Table 2). The very dry, low-θ_e layer above the CBL was interspersed with moist pockets above the dryline, above ~3000 m AGL (Fig. 16a). This moisture resulted from the upwelling of CBL air above the dryline [as encountered by chance along the 3.2 km AGL WKA flight leg at 2104 UTC (section 4d)], and/or the advection of high-θ_e air detrained from deep convection that formed earlier to the south along the dryline. The latter mechanism is speculative, but is supported by the wind direction above the CBL, roughly parallel with the dryline. The LCL came close to the LFC above the dryline (Fig. 16), resulting in near-zero CIN (Table 1). Where the sounding CIN vanishes, emerging CBL plumes are more likely to survive the buoyancy-destroying effect of entrainment in an environment that is more humid, in other words the moistening of the dry free troposphere conditions it for CI. It is not clear whether this conditioning was significant in this case, that is, whether it explains the lack of CI at 2040 UTC [when the CIN first became near zero (section 4d)] and the presence of CI an hour later.

The dropsonde transect suggests that the upwelling CBL air primarily was moist air (i.e., emerging from the east side of the dryline), in terms of conserved properties such as θ_e and r_v. This is consistent with the southerly inflow jet observed on the moist side [e.g., in the 2128 UTC sounding (Fig. 16)], and with the WCR observations along the last two flight legs (Figs. 13d,e, and

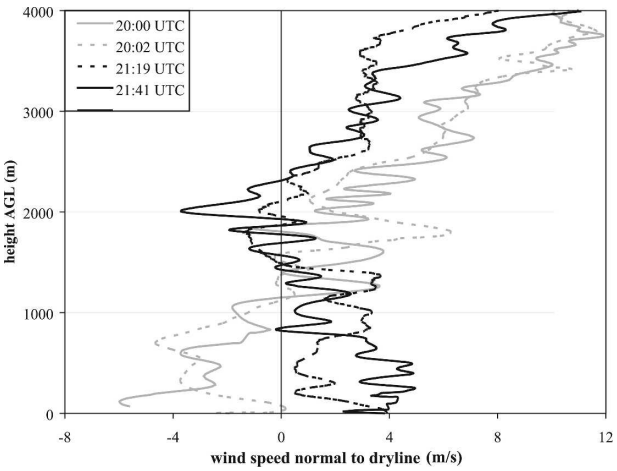

FIG. 15. Lower-tropospheric wind profiles normal to the dryline, derived from radiosonde data. The radiosondes are chosen to represent ambient conditions "ahead" (i.e., on the opposite side of the dryline) of the solenoidal circulation. The 2000 and 2002 UTC profiles are from the east side since the dryline tilts back to the west, and the 2119 and 2141 UTC soundings are from the west side soundings since the dryline is a more classic eastward-tilting boundary.

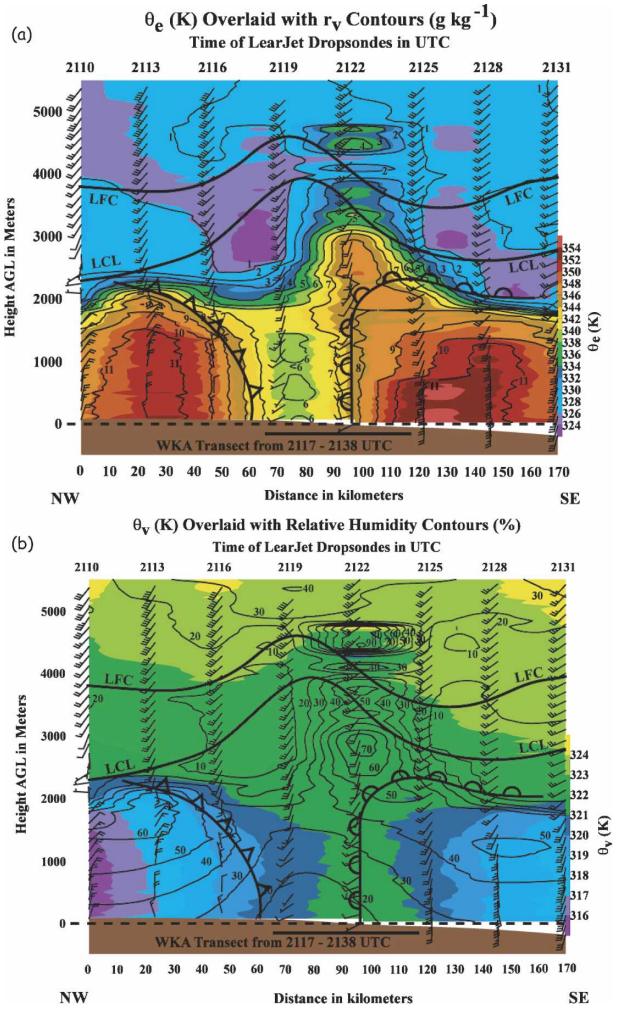

FIG. 16. (a) The θ_e (K) superimposed by contours of r_v (g kg^{-1}) and (b) θ_v (K) superimposed by contours of relative humidity (%), interpolated from a series of eight Learjet dropsondes. Dropsonde release times are denoted at the top of the transects. Winds are plotted as wind barbs along the vertical dropsonde line. The bold solid lines connect the LCL and LFC for each sounding. The bold solid line near the bottom shows the location of the third WKA stepped traverse (Fig. 12). Approximate locations (and slopes) of the cold front and dryline are shown.

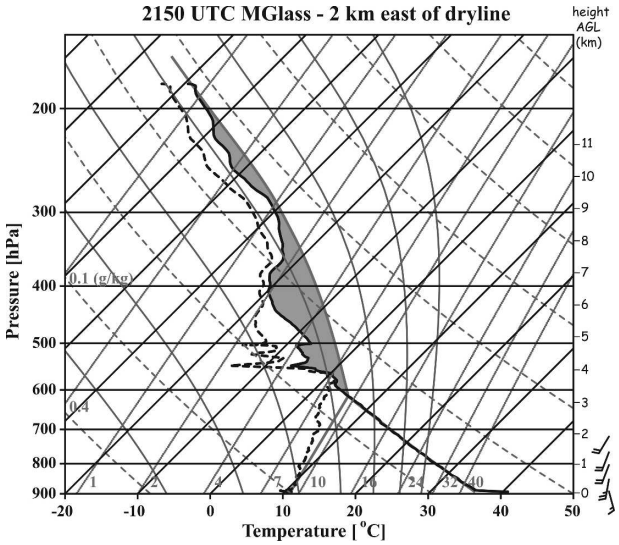

FIG. 17. Sounding released at 2150 UTC ~1.5 km east of the dryline, plotted on a skew T–log$p$. The solid (dashed) bold line denotes the observed temperature (dewpoint). The solid gray lines represent the temperature and dewpoint of a parcel lifted from the surface. The gray area visualizes the CAPE in this sounding. Clearly the LFC coincides with the LCL and there is no CIN.

Figs. 9h,i). According to the 2125 UTC dropsonde (~23 km east of the dryline; Fig. 16a), the boundary layer r_v averaged 10.5 g kg^{-1}, which is higher than in earlier moist-side soundings (e.g., the 2002 UTC sounding at the same distance from the dryline; Table 1). This increase in r_v suggests positive moisture advection by the southerly low-level jet in this region.

On the scale of the dropsonde transect, the DCZ was buoyant relative to both the moist air mass and the postfrontal air (Fig. 16b). Thus, on this scale both the dryline and the cold front would propagate as density currents, approaching each other. In fact the dryline and cold front approached each other (M06). Convective outflows within the moist air mass may have contributed to this evolution.

At the latitude of the WKA transects, towering cumulus develop above the dryline around 2130 UTC. A sounding released at 2150 UTC just to the north of the WKA transect line, ~1 km east of the dryline, had zero CIN (Fig. 17). The CBL, roughly 3500 m AGL deep (Table 1), was not yet modified by convective downdrafts, but the air above the LFC had been moistened and warmed significant by cumulus detrainment nearby, resulting, for instance, in a superadiabatic layer near 560 hPa. The radiosonde entered a growing anvil near 400 hPa.

5. Discussion

a. Solenoidal circulation

Several studies have documented a θ_v difference of 1–2 K across the dryline (e.g., McCarthy and Koch 1982; Parsons et al. 1991; Ziegler and Hane 1993; Atkins et al. 1998). The scale at which this difference is assessed varies, but in all cases the dry air mass is lighter. Several studies even mention the similarity of a dryline with a density current, driven by the denser CBL air on the moist side (Parsons et al. 1991; Ziegler and Hane 1993; Bluestein and Crawford 1997; Atkins et al. 1998). Our observations indicate that the local θ_v difference across the dryline is rather small, generally

less than 1 K (5 km)$^{-1}$, much less than typically observed across a well-defined density current (e.g., Geerts et al. 2006). To our knowledge no other study has documented a nonclassical early phase (where the dry air mass is more dense), nor a reversal of the θ_v gradient. In this study, we examine the tilt of the dryline echo plume from vertical. Such tilt suggests a thermally direct solenoidal circulation in accordance with the observed θ_v gradient, and its reversal. This circulation is further corroborated by VPDD transects, especially the one at 2015 UTC (Fig. 10a). The early westward-tilting phase is unusual, and may relate to larger-scale baroclinicity in this case.

Is the observed horizontal gradient of θ_v in the CBL sufficient to generate a solenoidal circulation? Convective updrafts in the CBL are driven by small-scale θ_v anomalies with an amplitude of 0.1–1 K (e.g., Miao et al. 2006). A horizontal gradient of buoyancy B generates horizontal vorticity η (e.g., Rotunno et al. 1988):

$$\frac{D\eta}{Dt} \cong -\frac{\partial B}{\partial x} \cong -\frac{g}{\theta_v}\frac{\partial \theta_v}{\partial x}. \quad (1)$$

Here D/Dt is the total derivative and x the direction of the buoyancy gradient. WCR transects described in section 4 suggest that the scale of this vorticity, or solenoidal circulation, is O(2 km), and that $\Delta\theta_v/\Delta x$ is on the order of 0.5 K (2 km)$^{-1}$ across the dryline. We assume a 2 m s^{-1} circulation over a 2-km length scale in both dryline-normal and vertical directions. According to (1), such circulation can be generated rapidly ($\Delta t \approx$ 8 min) by the observed θ_v gradient. This time scale is nearly one order of magnitude less than the circulation period itself. This suggests that the observed θ_v gradient suffices. The observed circulation reversal in response to a buoyancy reversal confirms the short time scale of baroclinic vorticity generation. Surface friction decelerates this generation and makes the circulation asymmetric, with a narrow zone of convergence and tilted ascent (e.g., Xue et al. 1997). This tilt is not due to ambient shear. The resulting boundary will propagate toward the less dense air at a speed that depends on the pressure gradient (which the WKA did not measure) and thus on $\Delta\theta_v$ (which we did measure), assuming hydrostatic balance. For a fine line to occur, updrafts and convergence need to be sustained (Geerts and Miao 2005a), and this persistent convergence toward the fine line, evident in the WKA and DOW3 data, in turn sustains the density gradient that the solenoidal circulation aims to destroy.

The tilt of the solenoidal ascent may compromise the ability of buoyant parcels to reach the LCL and LFC. In the presence of ambient shear, vorticity balance across a density gradient may result in more vertically oriented updrafts (Rotunno et al. 1988; Weisman et al. 1988). Specifically, this theory [known as the Rotunno–Klemp–Weisman (RKW) theory, recently revisited in Weisman and Rotunno (2004)] suggests that upright vertical motion is favored when the baroclinically generated horizontal vorticity along the boundary is opposite and about equal to the horizontal vorticity associated with line-normal wind shear over the depth of the density current, about 2 km in our case. The theory was developed to explain squall-line longevity, but it has been used also to explain CI (Wilson et al. 1992).

Some ambient wind profiles across the dryline are shown in Fig. 15. Both before and after the reversal of the solenoidal circulation, the ambient horizontal vorticity in the lowest 2 km points opposite to the baroclinically generated horizontal vorticity, that is, to the north during the westward tilt phase (westerly shear; gray profiles in Fig. 15), and to the south during the eastward tilt phase (easterly shear in the lowest 2 km; black profiles in Fig. 15). This is remarkable, but consistent with the CBL deepening near the dryline (Fig. 6), and with the increasing low-level confluence and upper-CBL diffluence (Table 2). The magnitude of the ambient vorticity, $(\partial u_n/\partial z)$, where u_n is the wind component normal to the dryline, is about 3 m s^{-1} km^{-1} or 3×10^{-3} s^{-1} (Fig. 15), while the solenoidal vorticity described above (2 m s^{-1} circulation along a square box 2 km wide) is a comparable 4×10^{-3} s^{-1}. Therefore the ambient shear appears conducive to erect updrafts and CI throughout the observation period.

Thus, the finescale solenoidal circulation may have contributed to the observed CBL deepening and CI. We do not argue that the boundary layer convergence in the vicinity of the dryline, as documented by mobile mesonet, DOW3 Doppler velocity, and WKA gust probe data, is entirely due to density current dynamics. Mesoscale analyses clearly indicate that the dryline corresponds to a larger-scale wind shift and convergence line: strong southerly flow east of the dryline veers to weaker southwesterly flow on the dry side (Fig. 3). Thus, the genesis of this dryline needs to be interpreted at a scale at which the earth's rotation matters and the wind and pressure fields cannot be explained by density current dynamics. The larger-scale synopsis was discussed in section 2.

We do argue that the finescale convergence leading to a radar fine line and a humidity discontinuity is baroclinically induced. This convergence deepened the CBL in the DCZ (Fig. 6), leading to CI. This is consistent with previous interpretations (e.g., Anthes et al. 1982; Wilson et al. 1992; Ziegler and Rasmussen 1998). Convergence due to a solenoidal circulation operates on

finer scales and leads to the sharp humidity contrast observed by the WKA. Certainly the mesoscale moisture convergence was essential to CI in the 19 June case: the southerly flow ahead of the dryline gradually increased, up to 15 m s^{-1} at 250 m AGL just prior to CI (2128 UTC sounding in Fig. 16). Table 2 documents the associated increase in airmass and moisture convergence near the dryline. The finescale changes in dryline vertical structure, documented in this study, may have contributed to CI, in the sense that the interaction of the solenoidal circulation with the ambient shear led to deeper BL convection.

b. CBL doming above the dryline

Sounding data, MIPS wind profiler data, and WCR reflectivity profiles all agree that the CBL was higher above the dryline than on either side of it (Fig. 6). The dropsonde transect (Fig. 16b) and the 3.2 km AGL WKA flight leg at 2104 UTC (section 4d) show that this CBL "dome" above the DCZ, at heights above the ambient z_i (between about 2.2 and 3.2 km AGL), was associated with a negative θ_v anomaly, compared to either side of the dryline. This is confirmed by MIPS data (Fig. 18). The anomaly is small (<0.6 K according to all three sources), but it suggests that at the scale at which the "environment" is defined (15–50 km) and at the time of the observations (all within 30 min of CI), the dome was not a spontaneous growth (i.e., the thermals within had overshot their equilibrium level). In other words, the low-level convergence in the DCZ was not driven by convection, even immediately prior to CI, and was necessary for CI to occur. A remarkable observation in Fig. 6 is the rapid increase of $z_{i,\mathrm{th}}$ near the dryline during the last 30 min before CI, in other words this CBL dome appears to rise in altitude. The CI occurred at the time that this dome reached the LFC. About an hour before CI, the local atmosphere may have been close to CI, as suggested by a sounding (2040 UTC; Table 1) and wind profiler data (Fig. 5).

Closer inspection of Fig. 6 reveals a disagreement between three sources about the value and the change of z_i. This discord is largely due to different measurement principles (see section 2), and is large because the CBL was poorly capped. The 915-MHz enhanced signal-to-noise ratio (SNR) (KK06) is generally above $z_{i,\mathrm{th}}$. This appears to be due to a humidity gradient just above $z_{i,\mathrm{th}}$, evident in some soundings, or to the occasional penetration of a thermal above $z_{i,\mathrm{th}}$ [as intercepted by the WKA on 2104 UTC (section 4d)]. WCR data do capture a CBL depth increase, on both sides and above the dryline, until 2005 UTC (Fig. 6). During this time WCR echo plumes on the moist (east) side penetrated slightly higher than those on the west (dry) side. Possibly this is related to the higher temperature on the moist side. But z_{i_WCR} estimates near the time of CI are essentially the same as 1.5 h earlier, and they are much lower than $z_{i,\mathrm{th}}$: the WCR echo plumes did not capture the rapid deepening of the CBL dome prior to CI.

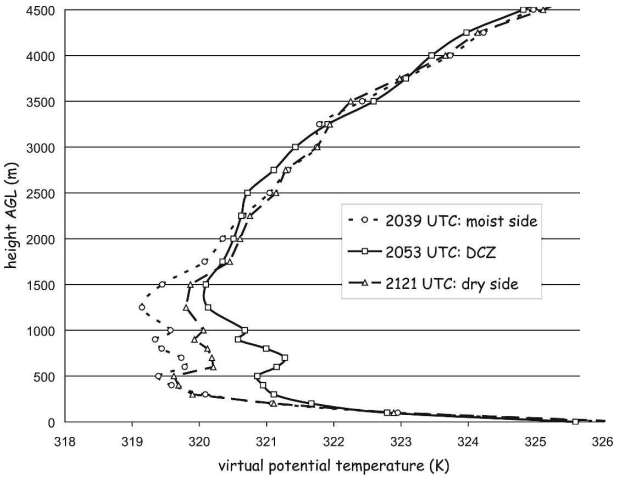

FIG. 18. Profiles of θ_v (K) derived from the MIPS 12-channel profiling radiometer, at 2039 (just east of the dryline), at 2053 (within the DCZ), and at 2121 UTC (just west of the dryline).

This suggests that echo plumes do not always rise to the mixed-layer top. This contrasts with WCR observations in the fair-weather, well-capped CBL: Miao et al. (2006) found good correspondence between z_{i_WCR} and $z_{i,\mathrm{th}}$, and found that echo plumes reasonably represent "thermals" [i.e., plumes of initially buoyant, rising air (Stull 1988, p. 461)]. All WCR transects shown in this study illustrate echo plumes in the DCZ. Plumes did occur outside the DCZ; although these plumes were generally weaker and smaller than those marking the dryline, their peak vertical velocities rivaled the DCZ plumes. Profiler data indicate that the magnitude and duration of updrafts in the 19 June DCZ were about twice that of updrafts associated with BL eddies away from the DCZ (KK06).

Very few WCR echo plumes reached above 2000 m on 19 June. This is consistent with MIPS wind profiler data, which show echo plumes (presumably insects in thermals) to be limited to about 2.0–2.5 km in height, much lower than enhanced SNR layer at 3.5 km between 2045 and 2100 UTC (KK06). It also chimes with observations from scanning centimeter-wave radars: the dryline fine line becomes better defined in the 2.5 h prior to CI both in DOW3 and Goodland WSR-88D reflectivity imagery, but the depth of the fine line does not change much: volume reflectivity data indicate that the fine-line echo vanishes between 1.5 and 2.0 km AGL during this period.

If this observation applies generally to CI along fine-line convergence lines, then the implication is that fine lines do not suddenly deepen before CI (i.e., that they cannot be seen suddenly over greater ranges in the lowest-elevation scan of operational radars, or at higher elevation angles). In other words, fine lines do not seem to harbor a CI precursor signature. From a nowcasting perspective, this is unfortunate. The reason why insect plumes do not extend to the full depth of $z_{i,\mathrm{th}}$ prior to CI may be temperature related: insects tend to fall out when the ambient air temperature falls below a threshold (e.g., 17°C), in this case ~2000 m AGL (Geerts and Miao 2005b). That thermals penetrate higher than the echo plumes is suggested by the WCR vertical velocity structure in the last three WKA transects (Figs. 9g–i and 13): the updraft seems to peak near the highest echoes, where the insect density becomes too small. In the earliest WKA transects (Figs. 8 and 9e,f), the vertical velocity maxima occurred well below the highest detectable echo level.

What matters to CI is less the kinetic energy of buoyant plumes in the CBL, but rather the depth of the CBL, and the proximity of z_i to the LFC (Foote 1984; Crook 1996; Ziegler and Rasmussen 1998). Mesoscale processes (such as a solenoidal circulation) are essential for this deepening, even though they are slower than convective-scale overturning. CBL deepening due to sustained convergence is enhanced when the CBL is poorly capped. A dome in a strong cap is statically unstable (negative θ_v anomaly) and the resulting hydrostatic surface pressure increase will oppose further convergence. On 19 June, the cap became very weak (Table 1). As discussed above, the CBL dome near 3000 m AGL is slightly negatively buoyant, but this negative θ_v anomaly is far smaller than the positive one below. Thermals along the dryline penetrated to an increasing depth, detraining CBL air in the dome. If the wind component normal to the dryline in the free troposphere just above the CBL is weak, this layer can be conditioned for CI through water vapor detrainment. Such preconditioning may have occurred during a ~1-h period prior to CI.

6. Conclusions

This study describes the finescale, mainly vertical structure of a prefrontal dryline on 19 June 2002 during IHOP_2002, mainly by means of airborne data collected along dryline traverses and simultaneous airborne radar echo and vertical velocity profiles. The following conclusions are drawn:

- Low-level mass and moisture confluence leads to an increasing definition of the dryline in terms of echo structure and humidity contrast, and to an increase in CBL depth in the DCZ. Local updrafts of 5–10 m s^{-1}, often collocated with anomalously high values of θ_v, are observed at most dryline intercepts during the 2.5-h intensive observation period.
- The vertical tilt of the echo plumes and single- and dual-Doppler velocity transects reveal a solenoidal circulation across the dryline, in agreement with the local horizontal density difference (i.e., the circulation is thermally direct).
- The difference in CBL depth and θ_v on opposite sides of the dryline, as well as the dryline slope and the sign of the solenoidal circulation, all reversed during the 2 h prior to CI. Initially the moist side had a higher θ_v (less dense), but later denser air occurred on the moist side. The latter phase, associated with a deeper CBL on the dry side, an eastward dryline slope, and a solenoidal vortex pointed north, appears to be a classical dryline configuration. To our knowledge, the former phase and the reversal process have not been documented elsewhere. The dryline decelerated and eventually retrograded, consistent with the buoyancy reversal. Just prior to CI the center of the solenoidal circulation appeared to move into the moist air, suggesting that the first towering cumuli were mostly fed by moist CBL air.
- The solenoidal circulation may have assisted the CBL deepening, as this vorticity was opposite to the vorticity of the wind shear on the opposite side of the dryline, both before and after the circulation reversal, but we cannot claim that it was essential to CI.
- Horizontal-plane WCR observations document intense finescale confluence and confirm the presence of misocyclonic echo cores.

Further work will examine the horizontal scale of the density difference that can drive a solenoidal circulation and associated low-level convergence and fine-line formation.

Acknowledgments. The National Science Foundation Grant ATMS0129374 supported this research. Sam Haimov was responsible for the WCR data collection. Rick Damiani developed the WCR Doppler velocity analysis package. Qun Miao generated Fig. 9. We appreciate the critical reviews by Chris Weiss and Kevin Knupp. Data for Fig. 18 were provided by Haldun Karan. We are grateful to all people that collected the IHOP_2002 data used herein, in particular the WKA, DOW3, MIPS, mobile sounding, and Learjet crews.

REFERENCES

Anthes, R. A., Y. H. Kuo, S. G. Benjamin, and Y.-F. Li, 1982: The evolution of the mesoscale environment of severe local

storms: Preliminary modeling results. *Mon. Wea. Rev.,* **110,** 1187–1213.

Arnott, N. R., Y. P. Richardson, J. M. Wurman, and E. M. Rasmussen, 2006: Relationship between a weakening cold front, misocyclones, and cloud development on 10 June 2002 during IHOP. *Mon. Wea. Rev.,* **134,** 311–335.

Atkins, N. T., R. M. Wakimoto, and C. L. Ziegler, 1998: Observations of the finescale structure of a dryline during VORTEX 95. *Mon. Wea. Rev.,* **126,** 525–550.

Benjamin, S. G., and T. N. Carlson, 1986: Some effects of surface heating and topography on the regional severe storm environment. Part I: Three-dimensional simulations. *Mon. Wea. Rev.,* **114,** 307–329.

Bluestein, H. B., and T. M. Crawford, 1997: Mesoscale dynamics of the near-dryline environment: Analysis of data from COPS-91. *Mon. Wea. Rev.,* **125,** 2161–2175.

Crawford, T. M., and H. B. Bluestein, 1997: Characteristics of a dryline passage during COPS-91. *Mon. Wea. Rev.,* **125,** 463–477.

Crook, N. A., 1996: Sensitivity of moist convection forced by boundary layer processes to low-level thermodynamic fields. *Mon. Wea. Rev.,* **124,** 1767–1785.

Damiani, R., and S. Haimov, 2006: A high-resolution dual-Doppler technique for fixed multi-antenna airborne radar. *IEEE Trans. Geosci. Remote Sens.,* **42,** 3475–3489.

Demoz, B., and Coauthors, 2006: The dryline on 22 May 2002 during IHOP_2002: Convective-scale measurements at the profiling site. *Mon. Wea. Rev.,* **134,** 294–310.

Doswell, C. A., III, and P. M. Markowski, 2004: Is buoyancy a relative quantity? *Mon. Wea. Rev.,* **132,** 853–863.

Ecklund, W. L., D. A. Carter, and B. B. Balsley, 1988: A UHF wind profiler for the boundary layer: Brief description and initial results. *J. Atmos. Oceanic Technol.,* **5,** 432–441.

Fankhauser, J. C., N. A. Crook, J. Tuttle, L. J. Miller, and C. G. Wade, 1995: Initiation of deep convection along boundary layer convergence lines in a semitropical environment. *Mon. Wea. Rev.,* **123,** 291–314.

Foote, G. B., 1984: A study of hail growth utilizing observed storm conditions. *J. Appl. Meteor.,* **23,** 84–101.

Geerts, B., and Q. Miao, 2005a: The use of millimeter Doppler radar echoes to estimate vertical air velocities in the fair-weather convective boundary layer. *J. Atmos. Oceanic Technol.,* **22,** 225–246.

——, and ——, 2005b: A simple numerical model of the flight behavior of small insects in the atmospheric convective boundary layer. *Environ. Entomol.,* **34,** 353–360.

——, R. Damiani, and S. Haimov, 2006: Fine-scale vertical structure of a cold front as revealed by airborne radar. *Mon. Wea. Rev.,* **134,** 251–272.

Hane, C. E., C. L. Ziegler, and H. B. Bluestein, 1993: Investigation of the dryline and convective storms initiated along the dryline: Field experiments during COPS–91. *Bull. Amer. Meteor. Soc.,* **74,** 2133–2145.

——, H. B. Bluestein, T. M. Crawford, M. E. Baldwin, and R. M. Rabin, 1997: Severe thunderstorm development in relation to along-dryline variability: A case study. *Mon. Wea. Rev.,* **125,** 231–251.

——, M. E. Baldwin, H. B. Bluestein, T. M. Crawford, and R. M. Rabin, 2001: A case study of severe storm development along a dryline within a synoptically active environment. Part I: Dryline motion and an Eta model forecast. *Mon. Wea. Rev.,* **129,** 2183–2204.

——, R. M. Rabin, T. M. Crawford, H. B. Bluestein, and M. E. Baldwin, 2002: A case study of severe storm development along a dryline within a synoptically active environment. Part II: Multiple boundaries and convective initiation. *Mon. Wea. Rev.,* **130,** 900–920.

Houze, R. A., 1993: *Cloud Dynamics*. Academic Press, 573 pp.

Jones, P. A., and P. R. Bannon, 2002: A mixed-layer model of the diurnal dryline. *J. Atmos. Sci.,* **59,** 2582–2593.

Karan, H., and K. Knupp, 2006: Mobile Integrated Profiler System (MIPS) observations of low-level convergent boundaries during IHOP. *Mon. Wea. Rev.,* **134,** 92–112.

Koch, S. E., and J. McCarthy, 1982: The evolution of an Oklahoma dryline. Part II: Boundary-layer forcing of mesoconvective systems. *J. Atmos. Sci.,* **39,** 237–257.

Lee, B. D., R. D. Farley, and M. R. Hjelmfelt, 1991: A numerical case study of convection initiation along colliding convergence boundaries in northeast Colorado. *J. Atmos. Sci.,* **48,** 2350–2366.

Leon, D., G. Vali, and M. Lothon, 2006: Dual-Doppler analysis in a single plane from an airborne platform. *J. Atmos. Oceanic Technol.,* **23,** 3–22.

Mahrt, L., 1977: Influence of low-level environment on severity of High-Plains moist convection. *Mon. Wea. Rev.,* **105,** 1315–1329.

McCarthy, J., and S. E. Koch, 1982: The evolution of an Oklahoma dryline. Part I: A meso- and subsynoptic-scale analysis. *J. Atmos. Sci.,* **39,** 225–236.

Miao, Q., B. Geerts, and M. LeMone, 2006: Vertical velocity and buoyancy characteristics of echo plumes in the convective boundary layer, detected by a profiling airborne radar. *J. Appl. Meteor. Climatol.,* **45,** 838–855.

Murphey, H. V., R. M. Wakimoto, C. Flamant, and D. E. Kingsmill, 2006: Dryline on 19 June 2002 during IHOP. Part I: Airborne Doppler and LEANDRE II analyses of the thin line structure and convection initiation. *Mon. Wea. Rev.,* **134,** 406–430.

Parsons, D. B., M. A. Shapiro, M. R. Hardesty, R. J. Zamora, and J. M. Intrieri, 1991: The finescale structure of a West Texas dryline. *Mon. Wea. Rev.,* **119,** 1242–1258.

Pazmany, A., R. McIntosh, R. Kelly, and G. Vali, 1994: An airborne 95 GHz dual-polarized radar for cloud studies. *IEEE Trans. Geosci. Remote Sens.,* **32,** 731–739.

Rotunno, R., J. B. Klemp, and M. L. Weisman, 1988: A theory for strong, long-lived squall lines. *J. Atmos. Sci.,* **45,** 463–485.

Schaefer, J. T., 1974: The life cycle of the dryline. *J. Appl. Meteor.,* **13,** 444–449.

Shaw, B. L., R. A. Pielke, and C. L. Ziegler, 1997: A three-dimensional numerical simulation of a Great Plains dryline. *Mon. Wea. Rev.,* **125,** 1489–1506.

Simpson, J. E., and R. E. Britter, 1980: A laboratory model of an atmospheric mesofront. *Quart. J. Roy. Meteor. Soc.,* **106,** 485–500.

Squires, P., and J. S. Turner, 1962: An entraining jet model for cumulonimbus updraughts. *Tellus,* **14,** 422–434.

Stull, R. B., 1988: *An Introduction to Boundary Layer Meteorology*. Kluwer Academic, 666 pp.

Sun, W.-Y., and Y. Ogura, 1979: Boundary-layer forcing as a possible trigger to a squall-line formation. *J. Atmos. Sci.,* **36,** 235–254.

——, and C.-C. Wu, 1992: Formation and diurnal variation of the dryline. *J. Atmos. Sci.,* **49,** 1606–1619.

Weckwerth, T. M., J. W. Wilson, and R. M. Wakimoto, 1996: Thermodynamic variability within the convective boundary

layer due to horizontal convective rolls. *Mon. Wea. Rev.,* **124,** 769–784.

——, and Coauthors, 2004: An overview of the International H_2O Project (IHOP_2002) and some preliminary highlights. *Bull. Amer. Meteor. Soc.,* **85,** 253–277.

Weisman, M. L., and R. Rotunno, 2004: "A theory for strong long-lived squall lines" revisited. *J. Atmos. Sci.,* **61,** 361–382.

——, J. B. Klemp, and R. Rotunno, 1988: Structure and evolution of numerically simulated squall lines. *J. Atmos. Sci.,* **45,** 1990–2013.

Weiss, C. C., H. B. Bluestein, and A. L. Pazmany, 2006: Fine-scale radar observations of the 22 May 2002 dryline during the International H2O Project (IHOP). *Mon. Wea. Rev.,* **134,** 273–293.

Wilson, J. W., and W. E. Schreiber, 1986: Initiation of convective storms at radar-observed boundary-layer convergence lines. *Mon. Wea. Rev.,* **114,** 2516–2536.

——, G. B. Foote, N. A. Crook, J. C. Fankhauser, C. G. Wade, J. D. Tuttle, and C. K. Mueller, 1992: The role of boundary layer convergence zones and horizontal rolls in the initiation of thunderstorms: A case study. *Mon. Wea. Rev.,* **120,** 1785–1815.

Xue, M., Q. Xu, and K. K. Droegemeier, 1997: A theoretical and numerical study of density currents in non-constant shear flows. *J. Atmos. Sci.,* **54,** 1998–2019.

Ziegler, C. L., and C. E. Hane, 1993: An observational study of the dryline. *Mon. Wea. Rev.,* **121,** 1134–1151.

——, and E. N. Rasmussen, 1998: The initiation of moist convection at the dryline: Forecasting issues from a case study perspective. *Wea. Forecasting,* **13,** 1106–1131.

——, W. J. Martin, R. A. Pielke, and R. L. Walko, 1995: A modeling study of the dryline. *J. Atmos. Sci.,* **52,** 263–285.

——, T. J. Lee, and R. A. Pielke Sr., 1997: Convective initiation at the dryline: A modeling study. *Mon. Wea. Rev.,* **125,** 1001–1026.